

**Evolution of a Cold Front Encountering Steep Quasi-2D Terrain:
Coordinated Aircraft Observations on 8-9 December 2001
during IMPROVE-2**

N.A. Bond¹, B.F. Smull², M.T. Stoelinga², C.P. Woods², A. Haase²,
and J.D. Locatelli²

¹ Joint Institute for the Study of the Atmosphere and Ocean
University of Washington
Box 354235
Seattle, WA 98195-4235

² Department of Atmospheric Sciences
University of Washington
Box 351640
Seattle, WA 98195-1640

For Publication in the *Journal of Atmospheric Sciences*

September 2004

Abstract

Research aircraft observations from the 8-9 December 2001 case of IMPROVE-2 describe the evolution of a wide cold frontal rainband (WCFR) during its passage from the Pacific coastline to a point 200 km inland over the Cascade Mountains of Oregon. This analysis has two primary objectives: (1) to examine how the terrain-induced changes in airflow, both near the surface and aloft, weakened the circulation associated with the WCFR, and (2) to show the resulting response in cloud microphysical properties such as liquid water content and ice particle concentrations. The kinematic structure of the WCFR is detailed using Doppler radar observations from a NOAA P-3 aircraft, while concomitant cloud microphysical properties are documented using flight-level measurements from the University of Washington Convair-580 aircraft. An accompanying MM5 control simulation (nested to a horizontal resolution of 4 km over the IMPROVE-2 domain) provides a meso-synoptic context and thermodynamic information to complement the aircraft observations. To the authors' knowledge, this case study represents the most complete documentation obtained to-date of the rapid modifications that may occur when a frontal rainband progresses from coastal waters into a region of prominent terrain..

1. Introduction

The mesoscale response of flow to orography is reasonably well understood in relatively simple situations where time-dependent and non-conservative effects are minimal. More complicated situations, such as landfalling storm systems, are not so amenable to simple interpretation. Nevertheless, current generation numerical weather prediction (NWP) models that have fine enough grid spacing to resolve mesoscale terrain appear to be capable of specifying the gross characteristics of the flow as fronts and other disturbances encounter prominent terrain (e.g. Colle et al. 1999a). While NWP models tend to handle these situations reasonably well in terms of the timing and intensity of the primary windshifts and temperature changes (given proper specification of the large-scale background flow), they do not simulate the distribution of precipitation nearly as reliably (e.g., Colle et al. 1999b). This deficiency constituted the overall motivation for the second phase of the Improvement of Microphysical PaRameterization through Observational Verification Experiment (IMPROVE-2).

A primary objective of IMPROVE (Stoelinga et al. 2003) was to collect the observations necessary to properly validate the bulk microphysical parameterization (BMP) schemes being used in present NWP models. The testbed for IMPROVE-2 was the Cascade Mountains of western Oregon. This region features a prominent, relatively 2D orographic barrier subject to the frequent passage of synoptic disturbances during the cool season, leading to copious precipitation. An impressive suite of observational assets was amassed for the field operations carried out in December 2001 (Stoelinga et al. 2003).

As in previous field programs that have examined cool-season precipitation in mountainous regions (such as the Sierra Project, IPEX, WISP, etc.), intensive observation periods during IMPROVE tended to focus on time periods of enhanced precipitation arising from a superposition of baroclinically forced ascent associated with mobile frontal systems and orographic ascent forced by substantial lower-tropospheric flow across the orographic barrier. The combination of these two dynamical influences can lead to highly complex evolution of cloud and associated microphysical processes influencing production of precipitation, particularly if the orography and frontal dynamics are themselves complex. A relatively simple situation, however, was provided by the 8-9 December 2001 case of IMPROVE-2, during which the orographic barrier and a cold front were both essentially two-dimensional in character and

roughly parallel in alignment. Moreover, the cold front maintained a reasonably steady and identifiable structure (in terms of slope, orientation, and motion) as it advanced from the Oregon coast to the lee of the Cascade Range. While the COAST project (Bond et al. 1997) involved research aircraft investigations of landfalling storm systems, those surveys were restricted to use of a single platform (the NOAA P-3) within the coastal domain and lacked comprehensive cloud microphysical measurements. By contrast, the 8-9 December IMPROVE-2 case offers an opportunity to detail multiple aspects of a front during its transit from the coastline to a point ~200 km inland over prominent terrain.

Our objective is to examine the evolution in mesoscale frontal structure and associated cloud microphysical properties and precipitation, with a focus on the circulation accompanying a wide cold-frontal rainband (WCFR; Matejka et al. 1980). The available data allow us to document how changes in kinematic structure relate to changes in the cloud microphysics, namely liquid water content, ice particle concentration and ice habit. These data are concentrated in the 2-5 km layer, which includes the core of the WCFR. Our results indicate that the WCFR rapidly weakened as it encountered the western, windward slope of the Cascade Mountains. From the perspective of the seeder-feeder mechanism (Hobbs et al. 1980) for generating precipitation in the vicinity of this WCFR, the orography appears to have had impacts on both seeder and feeder aspects. Most previous work regarding the effects of orography on fronts has focused on the changes occurring at lower levels; for the present case orographic effects on a front appear to also have been manifested well above the terrain. The potential causes of the weakening of the WCFR are explored including changes in conditional symmetric stability (CSI; Bennetts and Hoskins 1979) and the effects of a mountain-induced standing wave.

The primary data set for our analysis consists of the Doppler radar measurements collected by a NOAA P-3 research aircraft. The main source of cloud microphysical data are from the University of Washington's Convair-580 aircraft. Vertical profile information is used from operational and special balloon soundings and from a 915-MHz wind profiler. These observations are interpreted in conjunction with output from a numerical weather prediction (NWP) model, specifically the Penn State/NCAR MM5 model run quasi-operationally by the University of Washington. To our knowledge, this is the most complete data set ever collected detailing the evolution of a frontal rainband profoundly influenced by complex and prominent terrain immediately following landfall.

The organization of the paper is as follows. The next section outlines the data sets and methods used in the analysis. A synoptic overview of the case is then presented in Section 3. The bulk of the paper is comprised by Section 4, which consists of a detailed analysis of the evolution of the frontal zone and associated WCFR over the abruptly rising terrain of western Oregon. The dynamics underlying this evolution are discussed in Section 5. We conclude with a summary.

2. Data Sets and Methods

The principal objective of our analysis is to document evolution of the mesoscale flow and precipitation as the cold front/baroclinic zone of 8-9 December moved from the coast to over the Cascade Mountains. Our approach is to use the observations and model results in an integrated fashion. We rely heavily on the Doppler radar data collected by the NOAA P-3 and the cloud microphysical data collected by the UW Convair-580 research aircraft. These data sets, supplemented by other observational assets, offer an unprecedented opportunity to specify the evolution of a WCFR as it approaches and surmounts a major orographic barrier.

Flight tracks executed by the P-3 were designed to take advantage of the pseudo dual-Doppler synthesis technique described by Jorgensen and Smull (1993). Individual legs consisting of N-S tracks were executed along the primary axes of the coastal terrain, Willamette Valley and Cascade Mountains, shifting eastward with time to follow the primary band of precipitation inland (Fig. 1). The airborne Doppler radar data editing utilized the quasi-automated technique of Bousquet and Smull (2003), while, interpolation and synthesis of these data to yield volumetric analyses of wind and precipitation structure follow the procedures outlined by Yu and Smull (2000). The result is three-dimensional fields of horizontal and vertical winds, and radar reflectivity, on a grid with a spacing of 0.5 km in the vertical and 1.5 km in the horizontal, respectively, over multiple volumes each encompassing 75 by 135 km² in the horizontal and 7 km in the vertical, with the lowest analysis level located at 0.5 km (all heights are MSL). Because of the smoothing inherent to the synthesis, only horizontal variations at wavelengths >6-8 km are fully resolved. There are unavoidable limitations in the synthesis of Doppler radar observations over prominent terrain. First, editing of data to eliminate the influence of ground clutter implies that the synthesized wind and reflectivity fields are available

only to within 0.5 to 1.0 km of the surface. Second, the presence of an irregular lower boundary also introduces errors into estimates of the vertical velocity (w). For the present study, we therefore rely on the radar reflectivity and horizontal winds (which are relatively insensitive to errors in w) from the airborne radar in our descriptions of mesoscale structure.

The University of Washington's Convair-580 research aircraft executed two series of stacked horizontal legs to record flight-level state parameters and obtain measurements of cloud and precipitation microphysical properties during the passage of the WCFR through the study area. The purpose of these stack patterns was to gather measurements in a vertical cross section that was essentially orthogonal to the orientation of both the front and underlying orographic barrier. During IMPROVE-2, in southwesterly flow situations, the typical Convair-580 flight track was oriented roughly southwest to northeast (see Fig. 1) to approximately parallel the prevailing wind, and was executed from the top down to approximately follow the trajectories of falling precipitation. This "typical" plan was executed for the second flight stack (Fig. 1c), whereas the first stack (Fig. 1a) was executed using an alternate east-to-west climbing flight track (Fig. 1) as mandated by flight time constraints. However, due to the approximate two-dimensionality of both the orography and frontal system, we take both flight stacks to be representative of the cross-front/cross-mountain conditions over a substantial north-south length of the WCFR.

Output from a real-time run of the Penn State/NCAR MM5 NWP model is also used in analysis. The particular simulation we rely upon here is the run initialized at 0000 UTC 8 December, using output from NCEP's AVN (now GFS) model for initial and boundary conditions; very similar results were produced by the MM5 using NCEP's Eta model output for initial and boundary conditions. The output from the inner grid (4-km grid spacing) is utilized because of its better representation of the detailed orography, and presumably, its more realistic account of orographic effects. We do not present extensive diagnosis using the MM5 results, in part because of the wealth of direct measurements, but also because of the lack of fidelity of the MM5 simulation in some respects. In particular, as illustrated later, the MM5 simulation produced a stronger narrow cold-frontal rainband (NCFR) than was observed. This implies that the modeled circulation at the leading edge of the front, especially pertaining details in the vertical velocity near the surface, is not fully realistic. The modeled structure on the meso-synoptic scale does nonetheless appear reasonable, so we employ the MM5 output largely to

provide a context for the aircraft observations of radar reflectivities, winds and cloud microphysical properties in the vicinity of the WCFR.

3. Synoptic Overview

Our analysis concerns a lower to middle tropospheric cold front/baroclinic zone that moved inland from the Pacific Ocean into the Pacific Northwest late on 8 December 2001. The research aircraft observations constituting the foundation for our analysis were collected between about 2100 UTC 8 December and 0300 UTC 9 December. Here we concentrate on the larger-scale background conditions at 0000 UTC 9 December; much more detail on the mesoscale properties of this system, and in particular its evolution over the terrain of western Oregon, is provided in the following section.

The overall weather pattern during early December 2001 was one of westerly flow with a regular progression of vigorous synoptic disturbances. The 500 hPa map for 0000 UTC 9 December from NCEP (Fig. 2a) shows a short-wave trough approaching the Pacific Northwest. The axis of this trough was oriented NNE-SSW and was at about 130 deg.W nearing the coast of Oregon. The 850 hPa map at the same time (Fig. 2b) indicates a low-level baroclinic/frontal zone separating weak warm advection over western Oregon from stronger cold advection to the west. An infrared image from the GOES-W satellite at 0000 UTC 9 December (Fig. 3) shows a well-defined cloud band just ahead of the 500 hPa trough in the region of the low-level frontal zone. The open cellular convection over the ocean behind the principal cloud band was associated with the cooler, less statically stable air behind this frontal zone.

The mid-tropospheric trough accompanying this storm system began splitting at approximately the time it made landfall. In effect, the location of the greatest synoptic forcing of upward motion moved ashore well south of the study region. This is illustrated by maps of the quasi-geostrophic forcing of omega at 700 mb valid at 1800 UTC 8 December (Fig. 4a) and 0000 UTC 9 December (Fig. 4b). Predicted large-scale values of vertical velocity over the study region at the two times are comparable (-1.0 to -1.5 microbar/s), and thus synoptic-scale processes do not readily explain the observed rapid weakening of the WCFR (to be described further in Sec. 4). As will be shown, these significant changes in frontal structure occurred over an hour or two immediately following landfall; we will demonstrate that variations on this time

scale were due primarily to mechanisms acting on the mesoscale, and were likely related to the underlying orography.

The temporal changes in western Oregon associated with the cold front of 8-9 December 2001 are summarized using the observations from the 915-MHz wind profiler located at Irish Bend in the Willamette Valley (see Fig. 1). A time-height section of winds from this platform (Fig. 5) show a surface frontal passage at ~2100 UTC 8 December, as marked by a shift in the lowest kilometer from southwest winds of $\sim 15 \text{ m s}^{-1}$ to northwest winds of $5\text{--}7 \text{ m s}^{-1}$. Above roughly 1 km, this directional shift occurred progressively later with height. For example, the onset of the veering of the wind at 4 km, i.e., the leading edge of the frontal zone at that height, occurred at about 0300 UTC. Assuming a frontal propagation speed of the front was about 10 m s^{-1} (based on the progression of the primary precipitation and deep cloud band), the time-height section in Fig. 5 implies a frontal slope of about 1:70 in the 1-5 km layer.

The synoptic situation outlined above can be compared with the NWP guidance available at the time, in this case the 24 hour forecast from the operational MM5 run initialized at 0000 8 December. Here we compare the principal cloud band shown in Fig. 3 with its synthetic counterpart from the MM5 at the same time (Fig. 6). Note that the model has a band of cold cloud tops of the same scale and orientation as the principal cloud band. It does appear, however, that the modeled feature made landfall about 2 hours sooner than in reality. Comparisons between the observed and modeled wind fields confirm this small error in timing. In the MM5 results shown hereafter, a constant offset of two hours is thus used in comparisons of the model output to observations.

The synoptic conditions illustrated here represent a very common scenario in the Pacific Northwest during the cool season. A climatological study undertaken in planning for IMPROVE revealed that frontal passages occur at the Pacific Northwest coast on the average of 2.8 times a week. The cold front of 8-9 December was also of typical intensity in terms of wind speeds and precipitation rates. For example, the 12 hour rainfall amounts ending at 0600 UTC 9 December were about 0.7" on the central Oregon coast and about 0.1-0.2" in the Willamette Valley. Many of these types of fronts include one or more WCFRs. In the following section we carry out a detailed analysis of the flow and precipitation with the cold front of 8-9 December, with special attention focused on the evolution of a WFCR as the front moved over western Oregon.

4. Mesoscale Evolution of the Cold Front

a. Kinematic perspective

The P-3 research aircraft provided comprehensive coverage of the distributions of wind and precipitation as the cold front of 8-9 December transited western Oregon. The flight strategy consisted of following the primary band of precipitation from just offshore to the crest of the Cascade Mountains. Nine separate Doppler radar volumes all based on N-S oriented flight legs were synthesized, yielding three-dimensional fields of radar reflectivity (dBZ), meridional (v) and zonal (u) wind. Here we concentrate on the results from four Doppler volumes spaced roughly 45 minutes apart in time during the central portion of the flight. The front was oriented approximately north-south (actually NNE-SSW); east-west oriented vertical cross-sections therefore offer a compact means to illustrate the evolving frontal structure. The evolution of the front over the course of the flight (based on results from all nine radar volumes) is summarized in Table 1.

We begin with series of plan views of the radar reflectivity and winds at the 3.0 km level as the WCFR moved inland (Fig. 7). This progression illustrates the reduction in coverage of echo exceeding 20 dBZ at 3km in the vicinity of a windshift from southwest to west winds. Another notable change was a systematic increase in westerly component of the winds with time ahead of the windshift, and a concomitant decrease in westerlies behind the windshift. In other words, the convergence in the westerly component of the wind at 3km decreased with time following this band of precipitation.

Greater detail on the evolution of the WCFR is provided by sets of east-west vertical cross-sections of reflectivity (Figs. 8a-d), v (Figs. 9a-d) and u (Figs. 10a-d) bisecting the radar volumes for 2315, 2359, 0045 and 0129 UTC. While there are north-south variations in these volumes, these sections were found to represent the structure in the vicinity of the WCFR in general. The reflectivity sections show a decrease in the heights of the echo tops from about 6 km while the rainband was at the coast (Fig. 8a) to about 5 km when it was over the Cascades (Fig. 8d). In conjunction with this decline, a decrease in the magnitude of small-scale (~3-10 km) reflectivity perturbations occurred aloft in the vicinity of the WCFR. [Though not resolved

in the synthesized fields shown in Fig. 8, the signatures of these “generating cells” were more apparent in the raw sweep data (not shown).] Generating cells (e.g., Hobbs and Locatelli 1978; Matejka et al. 1980; and Houze et al. (1981), cause accelerated growth of ice particles within fallstreaks that extend to lower (and more moisture-rich) levels. This precipitation mechanism appears to have been more important when the WCFR initially came ashore than at later times, as also indicated in the cloud microphysical observations presented in Sec. 4c. The zone of enhanced reflectivity with the rainband tended to tilt westward with height in the coastal region (especially in the radar volume at 2225 UTC; not shown) and over the Willamette Valley (Fig. 8b). This tilt was appreciably reduced (or even reversed) once the rainband arrived over the west-facing slopes of the Cascades. The maximum reflectivities observed were ~ 33 dBZ while the rainband was near the coast. This maximum was just below 1 km and may have been associated with a bright band. Because of ground clutter issues mentioned earlier, the reflectivities near this level over the western slope of the Cascades are unknown. Shallow post-frontal convection began breaking out over the foothills of the Cascades during the latter half of the P-3’s survey, as suggested by Fig. 8c and especially by the last two radar volumes (not shown). The existence in the post-frontal environment of heavier precipitation over the first prominent rise in the terrain, rather than farther up the slope, is reminiscent of the pattern identified by Medina and Houze (2003) in the Alps, and can presumably be attributed to the low threshold of lifting required to trigger shallow convection in the presence of the reduced static stability within the post-frontal air mass.

The v-component flow sections (Figs. 9a-d) show that the vertical wind shear accompanying this rainband was prominent above 2 km. The v contours tilt noticeably westward with height behind the rainband. Over the rainband itself near the 3 km level, the orientation of these surfaces tended to tilt more with time, implying an increase of cyclonic vorticity. The Willamette Valley section (Fig. 9b) indicates a locally steep slope to baroclinic zone in the 3 to 4.5 km layer in the vicinity of the rainband, which is a characteristic signature of a WCFR (Matejka et al. 1980). There was a marked change at the level of 2 km and below behind the rainband from northerlies of ~ 6 m/s (Fig. 9a) to velocities of near zero (Figs. 9c-d). This change is consistent with the development of a barrier-induced southerly wind perturbation upstream of the Cascades, which effectively opposed synoptically-generated northerly flow at low levels.

Corresponding u-component flow analyses in Figs. 10a-d illustrate the changes in the

circulation approximately normal to the rainband during the period of interest. A thermally direct circulation (i.e., westerlies decreasing with height) embedded in roughly the 2 to 4 km layer is evident in the first two sections (Figs. 10 a-b) but absent in the latter two (Figs. 10c-d). The presence of multiple layers of forward and rearward flow relative to a front was also observed in the case studied by Browning et al. (2001). The first two sections indicate convergence in roughly the 2-3 km layer near the rainband overlaid by divergence in roughly the 3 to 4.5 km layer. A similar pattern was documented in the WCFR analyzed by Locatelli et al. (1994). The latter two sections have westerlies almost everywhere increasing with height, which given the slope of the u isolines signifies divergence in the plane of the section. The latter two sections also show deceleration of u at and behind the rainband at the lowest levels available, and acceleration of u near 3 km above the crest of the mountains.

As a means of summarizing the observed evolution of this rainband, the average values of various salient characteristics from each radar volume are listed in Table 1. For each volume, mean quantities were calculated based on east-west vertical sections along 44.75 °N, 44.5 °N (as shown in Figs. 8-10) and 44.25 °N. The quantities considered are the maximum height of the significant echo top (arbitrarily defined as the 9 dBZ level), the maximum shear in v over the layer of 2.5 to 4 km in the vicinity of the rainband, and the strengths of the upper and lower branches of the secondary circulation accompanying the WCFR defined as the minimum u in the 3.5 to 4.5 km layer and the maximum u in the 2 to 3 km layer, respectively. With regard to the secondary circulation, this feature was evident only at the first four radar analysis times. The indices recorded in Table 1 illustrate the marked decline in the rainband over the course of the P-3 radar survey. Particularly striking is the reduction in the cross-band circulation, as expressed in terms of the front-to-rear flow aloft relative to the rear-to-front flow at lower levels, that accompanied the WCFR's propagation toward the Cascade barrier.

b. Thermodynamic Perspective

There are fewer direct thermodynamic than kinematic measurements aloft, but available flight-level and weather balloon observations are sufficient to establish the veracity of thermodynamic fields simulated by MM5, which in turn may be used to describe broad aspects of the evolution of the cold front during its transit from the coast to the Cascade crest. Our focus

here is on the region of the WCFR near the 3 km level.

The horizontal structure of the front near the midpoint of the aircraft observation interval is summarized using air temperatures and vector winds from the MM5 at 2200 UTC 8 December (Fig. 11 a). The air temperatures show a difference of 3 to 3.5 °C across a zone of cyclonic shear over a distance of about 80 km. The modeled temperature difference is consistent with the flight-level air temperatures (T_a) measured by the P-3, which as mentioned above, decreased a comparable amount between 0045 UTC and 0216 UTC along the western flank of the Cascades. A map of cloud liquid water and vector winds at 1 km at 2200 UTC (Fig. 11b) shows that the model produced a sharp windshift at 1 km with a corresponding band of high liquid water. Essentially, the model simulation included a stronger signature of a NCFR in the low-level kinematic fields than was found in the radar data. The P-3 did observe a similarly oriented but broader band of enhanced radar reflectivities (and commensurately more gradual windshift) in this region near the S-Pol radar during its leg at 2359 UTC, which is again consistent with the model being about two hours fast in its timing of frontal passage over the experimental domain.

The evolution of the front over the course of the research aircraft flights is illustrated using east-west oriented vertical cross-sections of modeled equivalent potential temperature (θ_e) and water vapor mixing ratio (q_v). Plots of these model-derived quantities have been constructed along a cross section that corresponds closely to the P-3 Doppler radar results shown in the previous sub-section. The θ_e and q_v sections for 2000 UTC (Figs. 12a-b) indicate relatively warm and moist air in the lowest 2 kilometers just ahead of the simulated surface front, which at this time was just inland. The equivalent sections for two hours later (Figs. 13 a-b) show the overall baroclinity associated with this system, and a tongue of relatively high humidity sloping westward with height from the location of the surface front, which was now about one-third of the way up the western flank of the Cascades. The θ_e perturbations near and just downstream of the terrain crest (Fig. 13a) appear to be caused by mountain waves. The last pair of sections in this series is for the model time of 0000 UTC 9 December (Figs. 14a-b). The model solution positions the surface front about 50 km past the crest. The signature of the front or baroclinic zone in the 2-5 km level is best seen in the q_v field (Fig. 14b), which indicates substantial drying in the wake of the cross-frontal circulation aloft (not shown). An important point is that the MM5 results indicate that the thermodynamic conditions in the 2-4 km layer in the vicinity of the WCFR changed little during the period of intensive observations, even as precipitation rates

associated with this feature underwent significant changes. The specific humidity near the core of the WCFR did decrease by about 15%, but the vertical gradient in θ_e remained at a near constant value of about 4 K km^{-1} in a frame of reference moving with the front. This value is similar to that directly measured in the 2 to 4 km level from the 0000 UTC 9 December balloon sounding at Salem, OR (Fig. 15), which was virtually coincident with the WCFR's passage. More details about the kinematic and thermodynamic environments of this cold front are presented in Sec. 5, which discusses the dynamics of the evolution of the WCFR.

c. Cloud Microphysical Perspective

In keeping with the kinematic analyses presented previously, the Convair-580 flight paths and associated microphysical measurements are shown in east-west vertical cross sections (height-longitude plots) passing through the location of the ground-based “S-Pol” radar, which was located approximately at the center of the study area. The flight stacks themselves were not precisely in this cross section, but have been projected onto this vertical plane (Fig. 16). Also indicated is the terrain profile underlying the relevant Convair-580 flight stack.

The position of the cold frontal surface is also depicted in the cross sections in Fig. 16. The frontal position was located by identifying the robust frontal windshift in 915-MHz vertical wind profiles taken at Newport, Irish Bend (see Fig. 5), McKenzie Bridge, and Black Butte, Oregon, as well as VAD scans from the S-Pol radar near Sweet Home, Oregon (see Fig. 1 for locations). The frontal wind-shift signatures were then time-space adjusted and projected onto the cross sections shown in Fig. 16, leading to analyses of the positions of the frontal surface at 2225 UTC 8 Dec (panels a and c) and 0325 UTC 9 December (panels b and d). Flight-level wind and temperature data confirmed the frontal positions that were obtained from profiler and radar scans.

A difficulty arises in depicting measurements from an aircraft flight, which encompass several hours of elapsed time, when one is interested in features influenced by both a moving frontal boundary and fixed orography. Our approach here is to show the flight track in the ground-relative framework, with the frontal symbol representing the frontal position at the time the aircraft was located at the star symbol in each frame. While the front did move steadily during the course of each flight stack, this movement was small enough such that portions of the flight shown to be above (or below) the frontal surface were, for the most part, actually above (or

below) the frontal surface. The goal of each flight was to place the aircraft in the heart of the WCFR, and the tilt of each stack maintained the flight legs in roughly the same horizontal position relative to the front and the WCFR.

The first or "Coastal" Convair-580 flight probed the WCFR while it passed over the coastal mountains of western Oregon, when the surface front was ascending the windward slope of the Cascade Range; whereas the second of "Cascade" Convair-580 flight probed the WCFR while it was over windward slope of the Cascade range, by which time the surface front had progressed well into eastern Oregon. A comparison of the microphysical characteristics of the WCFR at these two times shows several interesting differences. In the liquid water content (LWC) field, which was measured with a PVM-100A optical sensor (Gerber et al. 1994), the Coastal flight (Fig. 16a) was characterized by values from $0.02\text{--}0.10\text{ g m}^{-3}$ throughout most of the depth of the rainband that was examined by the aircraft. These values are small, and in fact generally appeared to be the result of false detection of LWC in the presence of significant ice particle concentrations, as discussed by Evans et al. (2005). There were, however, several spikes in LWC observed during this coastal stack in which values exceeded 0.10 g m^{-3} , indicating the presence of active upward motion within generating cells encountered in this part of the rainband (Matejka et al 1980). A more robust patch of enhanced LWC is seen in Fig. 16a, near the uppermost reaches of this flight stack. The presence of mid-level convective cells (generating cells) near the top of the precipitating cloud while the rainband was near the coast was found in the radar data from the P-3 discussed earlier, and in scans from the ground-based S-Pol radar in a vertical cross section along the Convair-580 flight track (not shown). Representative examples of generating cells are shown in the Evans et al. (2005) case from IMPROVE-1.

The later Cascade flight stack (Fig. 16b) found nearly uniformly negligible ($< 0.025\text{ g m}^{-3}$) values of LWC throughout most of the flight stack, both above and below the frontal surface, indicating weak or nonexistent upward motion, as well as an absence of contamination due to the presence of significant ice particles. An exception is in the lowest leg of the Cascade flight, which followed the terrain from the crest of the Cascade Range to the Willamette Valley at an altitude of $\sim 1.5\text{ km}$ above ground level. During this leg, patches of high LWC (up to 0.25 g m^{-3}) were encountered. By examining scans from the S-Pol radar, it was determined that this lowermost leg of the Cascade flight was entirely behind the back edge of the WCFR, where radar echo

tops decreased in height from 8 km to 5 km. Thus, the patches of higher LWC in this leg are associated with purely orographic, shallow (albeit more convective) post-frontal clouds.

Ice particles were measured using a PMS 2D-C probe (Knollenberg 1976) on the Convair-580 aircraft. During the Coastal flight, particle concentrations ranged from 10-18 liter⁻¹ throughout the depth of the flight stack (Fig. 16c). The ice crystal habits encountered suggested active growth under conditions at or near water saturation at all levels: cold-type crystals falling from above at -17 °C; dendritic crystals at -15 °C; broad-branched crystals at -12 °C; radiating assemblages of plates at -7 °C; and needles, as well as needles aggregating with other crystals, at -5 °C. There was also a suggestion of rimed crystals in some locations such as those shown at the right (eastern-most) end of the flight leg at -12 °C. The increase in particle concentrations with decreasing altitude suggests the possibility that active ice enhancement was occurring, although conditions conducive to the riming-splintering mechanism (Hallett and Mossop 1974; Mossop and Hallett 1974) were not observed. In particular, few if any cloud droplets larger than 24 µm in diameter were seen at temperatures between -3° and -8°C.

Ice particle concentrations appear similar during the Cascade flight (Fig. 16d), although the regions of ice particles are more patchy. Ice particles seen in the upper legs were generally smaller than those seen in the Coastal flight. In addition, dendritic crystals were generally not seen in the middle part of this flight stack, indicating a lower degree of saturation (at least in the dendritic growth region of ~-15 °C) than in the previous stack. These observations indicate that the production of ice in the mid-troposphere was, on the whole, less vigorous during the Cascade flight than during the Coastal flight. In the lowest leg of the second Convair flight, the aircraft encountered regions of exclusively needles and aggregates thereof, as well as rimed aggregates and what appear to be liquid water droplets. This finding is consistent with purely orographic forcing of clouds and precipitation in the postfrontal lower troposphere behind the WCFR, as discussed above in regard to LWC for this lowest leg of the Cascade flight.

The region of significant concentrations of ice particles appears to extend to a higher altitude in the Cascade flight than in the earlier Coastal flight, but this is not inconsistent with our interpretation that precipitation production was more vigorous in the earlier flight. The Cascade flight was conducted above a higher portion of the frontal surface, and the cloud was deeper with colder cloud tops. This led to more numerous ice particles aloft, but as described above, these particles were generally smaller. In terms of impacts on actual precipitation production, this

influence can be seen more clearly if the average precipitation rate at the various flight levels is derived from the aircraft particle imagery. This is accomplished by using subjective particle habit identification and published mass-diameter and fallspeed-diameter relationships for the various habits, as explained in more detail in Woods et al. (2005). A vertical profile of the derived precipitation rates is shown for both flights in Fig. 17. The Coastal flight shows a steadily increasing precipitation rate with decreasing altitude, indicating (under steady-state assumptions) a situation of active growth, most likely due to vapor deposition considering the low availability of liquid water for riming. The Cascade flight, on the other hand, shows consistently small precipitation rates at all levels, indicating that on average, precipitation growth had slowed or even stopped by this time, at least in the region of frontally driven precipitation production. At lower altitudes, growth likely continued due to both riming and vapor deposition in the zone of terrain-forced upslope flow.

5. Possible Causes for Observed Weakening of the WCFR

The P-3 radar and Convair-580 cloud microphysical observations presented in Sec. 4 reveal that the WCFR weakened as it approached the Cascade Mountains. Here we explore mechanisms that could have contributed to this notably rapid evolution. Opportunity for such an examination is afforded by the availability of exceptionally detailed observations of the WCFR.

The formation of bands of precipitation in midlatitude storms, and in particular those bands oriented along the thermal wind vector, has been hypothesized to arise from the release of conditional symmetric instability or CSI (Bennett and Hoskins 1979; Emanuel 1983a), otherwise known as slantwise convection. The WCFRs observed during the University of Washington's CYCLonic Extratropical Storms (CYCLES) Project appear to have formed in an environment of CSI, and exhibit other attributes (e.g., a characteristic spatial scale) consistent with this mechanism (Parsons and Hobbs 1983a). Two-dimensional idealized NWP model simulations of a cold front by Knight and Hobbs (1988) revealed that precipitation bands resembling WCFRs formed and intensified in a region supporting CSI. Because CSI is thought to be important to WCFRs in general, it is interesting to examine whether it may help account for the evolution of

the rainband of the present case.

Slantwise convection occurs where the moist potential vorticity (MPV) is negative, which itself depends on the inertial and convective stability. Our analysis of the aircraft data and MM5 model output suggests that the temporal changes in the vicinity of the WCFR were more pronounced in the winds than in the thermodynamics as it moved from the Willamette Valley to the crest of the Cascades. For that reason, the focus here is on the evolution of the inertial stability, and in particular the distribution of absolute momentum (M), in the vicinity of the WCFR. To facilitate comparisons with the fields shown in Sec. 4, the east-west projection for vertical cross sections that is used in Sec. 4 is also used here. This orientation is approximately normal to the terrain and facilitates comparisons with the results shown in Sec. 4. While these sections are not exactly normal to the front and thermal wind vector, this effect is negligible in evaluation of the along-front flow. It is also assumed that the observed meridional wind represents a reasonably accurate proxy for the meridional geostrophic wind, which is actually the basic parameter that enters in to determination of M . Again, the objective is to document how the CSI at the WCFR changed in a qualitative sense, rather than to make quantitative estimates of the slantwise convective available potential energy (SCAPE).

The M distributions based on P-3 observations from the legs centered at 2225, 2359 and 0045 UTC are shown in Figs. 18-20. The first in this sequence (Fig. 18), when the WCFR was approaching the coast, includes pockets in the 2-4 km layer where M surfaces were flat or even tilting downwards to the left (i.e. west), indicating inertial instability assuming meridional gradients in u were negligible. The M surfaces tended to take on more of an upward tilt to the west as the WCFR advanced over the Willamette Valley and closer to the Cascade barrier (Fig. 19). This tendency continued as the WCFR was weakening during its eastward progression over the western flank of the Cascades (Fig. 20). The observed steepening of the M surfaces can be understood in terms of the change in the vertical shear of v , which is equal to the vertical derivative of M . The decrease in the strength of the northerlies below the frontal zone (as seen by the differences between Figs. 8c and 10c) resulted in a reduction of the vertical shear and thus a reduction in dM/dz . Such a reduction in dM/dz , with no change in vertical vorticity (the horizontal gradient in M), would imply a tilting of M surfaces towards the vertical and associated reduction of susceptibility to CSI-induced overturning.

The decrease in the low-level northerlies over the western slope of the Cascades may be

at least partly attributable to a barrier jet-like phenomenon (e.g., Parish 1982). This mechanism causes along-barrier flow down the pressure gradient within a Rossby radius of the barrier; in the present case development of a "southerly barrier jet" was strictly in a perturbation sense in that what occurred was a reduction in the strength of the post-frontal northerly winds. In its simplest expression, the formation of a barrier jet is a conservative process, and hence while it can lead to transports of MPV, it represents neither a source nor a sink of MPV, and therefore cannot change slantwise stability on its own. Any change in the slope of M surfaces due to this process alone would necessarily be accompanied by compensating changes in the slopes of θ_e surfaces that would preserve the degree of slantwise stability. Nevertheless, the potential exists for terrain to impact the MPV in a non-conservative manner. Variable terrain causes horizontal gradients in surface friction which in turn serves as a source of vertical vorticity; it is unknown whether this effect was significant in the present case. It seems likely that it was only of secondary importance, given that the core of the WCFR lay well above the surface. Gradients in surface friction would have to have been quite substantial to alter the wind fields significantly over a deep layer during the hour or two of WFCR weakening. As such, changes in the local environment's susceptibility to CSI-induced overturning do not appear to explain this evolution.

It does appear, however, that the WCFR was adversely impacted by a stationary mountain wave induced by the Cascade Mountains. One consequence of this wave was enhanced westerly winds in the layer from about 2.5 to 4 km over the crest of the Cascades, as pointed out in the previous section. The effects of the terrain on zonal winds accompanying the front are illustrated here using output from the MM5, since it presents a far more horizontally extensive view than radar-based depictions, and extends data into non-precipitating regions. The first section is for 2200 UTC (Fig. 21), when the front (as defined by a couplet of low-level convergence with divergence above) was beginning to ascend the west slopes of the Cascades. Note the region of enhanced u ($u > 21 \text{ m s}^{-1}$) in the 2-3 km layer extended more than 50 km upstream (west) of the crest, and was increasingly in direct opposition to the frontally-induced circulation (the latter being highlighted by arrows superimposed on Figs. 21-23). As the front approached this relatively more stationary terrain-induced circulation feature, zonal winds near the 3 km level ahead of the front accelerated. This acceleration is also apparent in the u analyses based on the P-3 radar data shown in Figs. 10b and 10d. The remnants of the WCFR lay over the Cascade crest at ~0000 UTC 9 December, and by this time the thermally-direct circulation in the

cross-frontal plane near the 3 km level was much reduced (Fig. 22). It is interesting that, at least as viewed in the MM5 simulation, the frontal circulation near 3 km re-invigorated somewhat as it advanced well downstream of the crest, as suggested by the u section for 0200 UTC (Fig. 23).

The changes seen in the flow associated with the WCFR of 8 December can be described in terms of the following conceptual model. As the WCFR approached the western slopes of the Cascades, there was the expected blocking and deceleration of the westerly post-frontal flow immediately upstream of the terrain, leading to convergence in the zonal flow component and a associated southerly down-gradient perturbation (expressed as a reduction of prevailing post-frontal northerlies) in the lowest 1 to 1.5 km. Meanwhile, acceleration of the westerly winds occurred aloft (~2.5 to 4 km) ahead of the WCFR as a result of what we interpret as interaction of the baroclinically-induced flow perturbation with a standing wave associated with flow over the Cascade Mountain barrier. Enhancement of westerly winds extending upstream of the crest is consistent with an estimated Froude number of roughly 0.5 and hence a subcritical hydrodynamic regime (e.g., Durran 1986). As such, it appears that both branches of the thermally direct frontal circulation were diminished by interactions with the terrain, but evidently via two distinct mechanisms. The forward motion of the cold, descending branch was impeded by terrain-induced low-level blocking of the cross-barrier flow, while rearward acceleration of the warm, ascending branch was counteracted by the enhanced westerly flow over and ahead of the Cascade crest induced by the mountain wave. The latter effect appears to have caused a reversal to rear-to-front flow ahead of the front at the level near the core of the WCFR. In other words, it appears that the stationary wave tied to the terrain helped cause the circulation at the WCFR to evolve from that characteristic of an anafront to that of a katafront (Sansom 1951), with a consequent decrease in upward motion at leading edge of the WCFR.

The occurrence of a frontal rainband weakening as it encountered the windward flank of a prominent barrier is not surprising. Previous theoretical (e.g., Gross 1994) and observational (e.g., Colle et al. 1999) studies have found frontolysis (frontogenesis) on the upstream (downstream) sides of barriers due to forced ascent (descent) and adiabatic cooling (warming) of the pre-frontal air mass. But these studies concerned fronts with prominent secondary circulations near the surface, and hence have some limitations in their applicability to the present frontal rainband, whose circulation core was aloft.

Parsons and Hobbs (1983b) included some information on changes in WCFRs as they

encountered terrain over the Pacific Northwest, and here we consider those results in the context of the present case. Their overall conclusion was that those WCFRs which they examined were not significantly impacted by topography, but their analysis was mostly limited to assessment of low-level reflectivities from a pair of ground-based radars, and of precipitation from a network of raingauges. Hence little information was available concerning how the accompanying frontal circulations evolved. Perhaps even more importantly, the most prominent terrain feature in their analysis domain was the quasi-circular Olympic Mountain. It seems likely that the response to such an obstacle would differ from that of a 2D barrier like the Cascade Mountains, as it likely would for a front intersecting the barrier more obliquely. It remains an open question whether most WCFRs exhibit a behavior similar to the case scrutinized here. Our results do bear on the mechanisms responsible for the enhancement of precipitation in general on the windward flanks of terrain after surface cold front passages in general. At least in the present case, and as suggested by the results from CYCLES, this enhancement is not due to WCFRs themselves, but rather more due to less-organized, shallow convection occurring farther behind the surface front.

6. Summary

Observations from a NOAA P-3 and the University of Washington Convair-580 aircraft during IMPROVE-2 have been used to describe the evolution of the cold front of 8-9 December 2001. The main precipitation feature accompanying this front was a WCFR, which weakened as it approached the steeply rising slopes of the Cascade Mountains. This weakening was especially pronounced in terms of the strength of a cross-frontal secondary circulation near the core of the WCFR, but was also manifested by decreases in the depth of echo top and the magnitude of the vertical shear in the along-frontal wind component. The decline in the vigor of the circulation with the WCFR resulted in about a four-fold decrease in liquid water content and a two-fold decrease in ice crystal concentration over a ca. 3h period immediately following its landfall. Slantwise convection or CSI has previously been implicated as an important forcing mechanism for WCFRs, and we examined the possibility that the terrain could have impacted the propensity for CSI—especially with regards to its inertial stability component. While noticeable changes in kinematic structure occurred as the front interacted with the terrain, compelling evidence of significant changes in the local environment's susceptibility to CSI was lacking in

this well observed case. On the other hand, both branches of the thermally direct frontal circulation in the vicinity of the weakening WCFR appeared to have been diminished by the terrain, albeit by superposition of two distinct mechanisms. Terrain blocking reduced the rear-to-front flow at low-levels beneath the front, and a stationary mountain wave enhanced the westerly winds aloft over and upstream of the crest, which effectively curtailed the front-to-rear flow above the front. The role of steeply rising terrain in inducing a reduction in the intensity of a baroclinically-induced precipitation feature by alteration of the midtropospheric flow field has thus been illuminated.

Acknowledgments - We appreciate the assistance provided by many of the scientific contingent of IMPROVE. Special thanks go to the flight crews of the NOAA P-3 and University of Washington Convair-580. Valuable contributions to data processing and display were provided by David Ovens and Stacy Brodzik. Kay Dewar assisted in preparation of Fig. 1. The manuscript was improved substantially following the constructive suggestions from three anonymous reviewers. Funding for IMPROVE was provided by the Mesoscale Dynamic Meteorology Program of the National Science Foundation, and by the U.S. Weather Research Program. This publication is funded by the Joint Institute for the Study of the Atmosphere and Ocean (JISAO) under NOAA Cooperative Agreement NA17RJ1232, Contribution 1050. Contribution 2682 of NOAA Pacific Marine Environmental Laboratory.

References

- Bennetts, D.A., and B.F. Hoskins, 1979: Conditional symmetric instability - a possible explanation for frontal rainbands. *Quart. J. Roy. Meteor. Soc.*, **105**, 945-962.
- Bond, N.A., C.F. Mass, B.F. Smull, R.A. Houze, M.-J. Yang, B.A. Colle, S.A. Braun, M.A. Shapiro, B.R. Colman, P.J. Neiman, J.E. Overland, W.D. Neff and J.D. Doyle, 1997: The Coastal Observation and Simulation with Topography (COAST) Experiment. *Bull. Amer. Meteor. Soc.*, **78**, 1941-1955.
- Bousquet, O., and B.F. Smull, 2003: Airflow and precipitation fields within deep Alpine valleys observed by airborne Doppler radar. *J. Appl. Meteor.*, **42**, 1497-1513.
- Browning, K.A., D. Chapman, and R.S. Dixon, 2001: Stacked slantwise convection. *Quart. J. Roy. Meteor. Soc.*, **127**, 2513-2536.
- Colle, B. A., C. F. Mass, and B. F. Smull, 1999a: An observational and numerical study of a cold front interacting with the Olympic Mountains during COAST IOP 5. *Mon. Wea. Rev.*, **127**, 1310-1334.
- Colle, B. A., K. J. Westrick, and C. F. Mass, 1999b: Evaluation of MM5 and Eta-10 precipitation forecasts over the Pacific Northwest during the cool season. *Wea. Forecasting*, **14**, 137-154.
- Durran, D.R., 1986: Another look at downslope windstorms. Part I: The development of analogs to supercritical flow in an infinitely, deep, continuously stratified fluid. *J. Atmos. Sci.*, **43**, 2527-2543.
- Emanuel, K.A., 1983a: The Lagrangian parcel dynamics of moist symmetric instability. *J. Atmos. Sci.*, **40**, 2368-2376.
- Emanuel, K.A., 1983b: On assessing local conditional symmetric instability from atmospheric soundings. *Mon. Wea. Rev.*, **111**, 2016-2033.
- Evans, A. G., J. D. Locatelli, M. T. Stoelinga, and P. V. Hobbs, 2005: The IMPROVE-1 storm of February 1–2, 2001. Part II: Cloud structures and the formation of precipitation. *J. Atmos. Sci.*, in press.
- Gerber, H., B. G. Arends, and A. S. Ackerman, 1994: New microphysics sensor for aircraft use. *Atmos. Res.*, **31**, 235-252.
- Gross, B.D., 1994: Frontal interaction with isolated orography. *J. Atmos. Sci.*, **51**, 1480-1496.
- Hallett, J., and S. C. Mossop, 1974: Production of secondary ice crystals during the riming process. *Nature*, **249**, 26–28.

- Hobbs, P.V., and J.D. Locatelli, 1978: Rainbands, precipitation cores and generating cells in a cyclonic storm. *J. Atmos. Sci.*, **35**, 230-241.
- Hobbs, P.V., T.J. Matejka, P.H. Herzegh, J.D. Locatelli, and R.A. Houze, Jr., 1980: The mesoscale and microscale structure and organization of clouds and precipitation in mid-latitude cyclones. I: A case study of a cold front. *J. Atmos. Sci.*, **37**, 568-596.
- Houze, R.A., Jr., S.A. Rutledge, T.J. Matejka and P.V. Hobbs, 1981: The mesoscale and microscale organization of clouds and precipitation in midlatitude cyclones. Part III: Air motions and precipitation growth in a warm-frontal rainband. *J. Atmos. Sci.*, **38**, 639-649.
- Jorgensen, D. P., and B. F. Smull, 1993: Mesovortex circulations seen by airborne Doppler radar within a bow-echo mesoscale convective system. *Bull. Amer. Meteor. Soc.*, **74**, 2146-2157.
- Knight, D.J., and P.V. Hobbs, 1988: The mesoscale and microscale structure and organization of clouds and precipitation in midlatitude cyclones. Part XV: A numerical modeling study of frontogenesis and cold-frontal rainbands. *J. Atmos. Sci.*, **45**, 915-930.
- Knollenberg, R. G., 1976: Three new instruments for cloud physics measurements: The 2-D spectrometer, the forward scattering spectrometer probe, and the active scattering aerosol spectrometer. *Preprints Int. Conf. Cloud Physics.*, Boulder, Amer. Meteor. Soc., 554-561.
- Locatelli, J.D., J.E. Martin and P.V. Hobbs, 1994: A wide cold-frontal rainband and its relationship to frontal topography. *Quart. J. Roy. Meteor. Soc.*, **120**, 259-275.
- Matejka, T. J., R. A. Houze, Jr. and P. V. Hobbs, 1980: Microphysics and dynamics of clouds associated with mesoscale rainbands in extratropical cyclones. *Quart. J. Roy. Meteor. Soc.*, **106**, 29-56.
- Mossop, S. C., and J. Hallett, 1974: Ice crystal concentration in cumulus clouds: Influence of the drop spectrum. *Science.*, **186**, 632-634.
- Medina, S., and R. A. Houze, Jr., 2003: Air motions and precipitation growth in Alpine storms. *Quart. J. Roy. Meteor. Soc.*, special MAP issue, **129**, 345-371.
- Parsons, D. B., and P. V. Hobbs, 1983a: The mesoscale and microscale structure and organization of clouds and precipitation in midlatitude cyclones. XI: Comparisons between observational and theoretical aspects of rainbands. *J. Atmos. Sci.*, **40**, 2377-2397.
- Parsons, D. B., and P. V. Hobbs, 1983b: The mesoscale and microscale structure and organization of clouds and precipitation in midlatitude cyclones. IX: Some effects of orography on rainbands. *J. Atmos. Sci.*, **40**, 1930-1949.

- Sansom, H.W., 1951: A study of cold fronts over the British Isles. *Quart. J. Roy. Meteor. Soc.*, **77**, 96-120.
- Stoelinga, M. T., P. V. Hobbs, C. F. Mass, J. D. Locatelli, B. A. Colle, R. A. Houze, Jr., A. L. Rangno, N. A. Bond, B. F. Smull, R. M. Rasmussen, G. Thompson, and B. R. Colman, 2003: Improvement of Microphysical Parameterizations Through Observational Verification Experiments (IMPROVE). *Bull. Amer. Meteor. Soc.*, **84**, 1807-1826.
- Woods, C. P., M. T. Stoelinga, J. D. Locatelli, and P. V. Hobbs, 2005: Microphysical processes and synergistic interaction between frontal and orographic forcing of precipitation during the December 13, 2001 IMPROVE-2 event over the Oregon Cascades. *J. Atmos. Sci.*, conditionally accepted.
- Yu, C.- K., and B. F. Smull, 2000: Airborne Doppler observations of a landfalling cold front upstream of steep coastal orography. *Mon. Wea. Rev.*, **128**, 1577-1603.

Table 1 Selected Characteristics of Rainband from each Radar Volume

Time	Echo Top (km)	Max. Shear (m/s)	Upper Branch (m/s)	Lower Branch (m/s)
2225	5.7	18	7.8	21.5
2315	5.3	19	8.5	21.3
2359	5.3	17	7.8	15.0
0021	4.8	17	5.7	10.0
0045	4.8	17	N.A.	N.A.
0105	4.9	15	N.A.	N.A.
0129	4.5	14	N.A.	N.A.
0155	4.3	12	N.A.	N.A.
0216	4.0	11	N.A.	N.A.

Notes: The echo top was defined as the height of the the 9 dBZ surface, the maximum shear was considered over the layer from 2.5 to 4 km, the magnitude of the upper branch was evaluated as the minimum zonal velocity in the 3.5 to 4.5 km layer, and the magnitude of the lower branch was evaluated as the maximum u in the 2 to 3 km layer. All quantities are for regions in the vicinity of the rainband and constitute averages over the three east-west sections along 44.75°N, 44.50°N, and 44.25°N.

Figure Captions

Fig. 1. Fig. 1 Flight tracks for NOAA P-3 (white lines) and University of Washington Convair-580 (gray lines) research aircraft during the IMPROVE-2 mission of 8-9 December 2001. Shading indicates terrain height, with the darkest N-S oriented band through Irish Bend locating the Willamette Valley, and lighter shading to east indicating the Cascade Mountains. Panels (a), (b) and (c) refer to roughly the first quarter, middle half, and last quarter, respectively of the P-3's mission.

Fig. 2a 500 hPa chart for 0000 UTC 9 December 2001 from the National Centers for Environmental Prediction (NCEP).

Fig. 2b As in Fig. 2a, but for 850 hPa.

Fig. 3 GOES-W infrared satellite image at 0000 UTC 9 December 2001.

Fig. 4a 700 hPa air temperature ($^{\circ}\text{C}$; red lines) and quasi-geostrophic omega (microbar s^{-1} ; black lines) for 1800 UTC 8 December 2001. Dashed (solid) omega contours indicate positive (negative) values at an interval of $0.5 \text{ microbar s}^{-1}$; zero contour is omitted.

Fig. 4b As in Fig. 4a, but for 0000 UTC 9 December 2001.

Fig. 5 Time-height section of winds from the 915-MHz wind profiler located at Irish Bend, OR (Lat: 44.36 N, Lon: 123.21 W, Elevation: 85 m). Time runs from right to left.

Fig. 6 Simulated IR satellite image valid at 0000 UTC 9 December based on cloud-top temperature from a 24-h forecast of the NCAR/Penn State MM5 numerical weather prediction model.

Fig. 7 Plan views of radar reflectivity (dBZ; see color table) and wind vectors at 3 km from the 2225 UTC, 2359 UTC and 0129 UTC 8-9 December radar volumes from the P-3 aircraft. Surrounding topography is shown as in Fig. 1, and range circles (20 km interval) centered on S-Pol radar are plotted for reference.

Fig. 8 Vertical cross-sections of radar reflectivity (dBZ) along 44.50 N from the (a) 2315, (b) 2359, (c) 0045 and (d) 0129 UTC P-3 radar volumes on 8-9 December 2001.

Fig. 9 As in Fig. 8, but for the meridional (v-component) wind (m s^{-1}).

Fig. 10 As in Fig. 8, but for the zonal (u-component) wind (m s^{-1}). Dashed and solid arrows refer to the front-to-rear and rear-to-front components, respectively, of the secondary circulation associated with the WCFR.

Fig. 11a Air temperature ($^{\circ}\text{C}$) at 3 km at 2200 UTC 8 December from the MM5. Black line indicates projection of vertical cross section shown in Figs. 12-14.

Fig. 11b As in Fig. 13a, but for cloud liquid water concentration (g kg^{-1}) at 1 km.

Fig. 12a Vertical cross-section of equivalent potential temperature (K) along 44.5 N at 2000 UTC 8 December from the MM5.

Fig. 12b As in Fig. 12a, but for water vapor mixing ratio (g kg^{-1}).

Fig. 13a-b As in Fig. 12a-b, but for 2200 UTC 8 December.

Fig. 14a-b As in Fig. 12a-b, but for 0000 UTC 9 December.

Fig. 15 Skew-T sounding from Salem, OR at 0000 UTC 9 December.

Fig. 16 Flight-level data for the 8-9 December 2001 from the University of Washington's Convair-580 aircraft. (a) Cloud liquid water (g m^{-3}) during the coastal flight (2151-2330 UTC). Flight-level temperatures ($^{\circ}\text{C}$) are also shown. Arrows indicate direction of track. (b) As in (a), but for the Cascade flight (0112-0442 UTC). (c) Ice crystal concentration (liter^{-1}) with sample PMS 2D-C imagery along the coastal flight legs. The vertical dimension of each sample ice crystal image strip is 800 microns. (d) As in (c) but for the Cascade flight.

Fig.17. Vertical profiles of precipitation rate (mm h^{-1}) for the Convair-580 Coastal and Cascade flights. Values are obtained for the horizontal flight legs seen in Fig. 16. For each flight leg, dots represent mean values and bars represent one standard deviation.

Fig. 18 Vertical cross-section of absolute momentum (m s^{-1}) along 44.50 N from the P-3 airborne Doppler radar analysis at 2225 UTC 8 December.

Fig. 19 As in Fig. 18, but for the 2359 UTC leg.

Fig. 20 As in Fig. 18, but for the 0045 UTC leg.

Fig. 21 Vertical cross-section of zonal wind (m s^{-1}) along 44.5 N at 2200 UTC 8 December from the MM5.

Fig. 22 As in Fig. 21, but for 0000 UTC 9 December.

Fig. 23 As in Fig. 21, but for 0200 UTC 9 December.

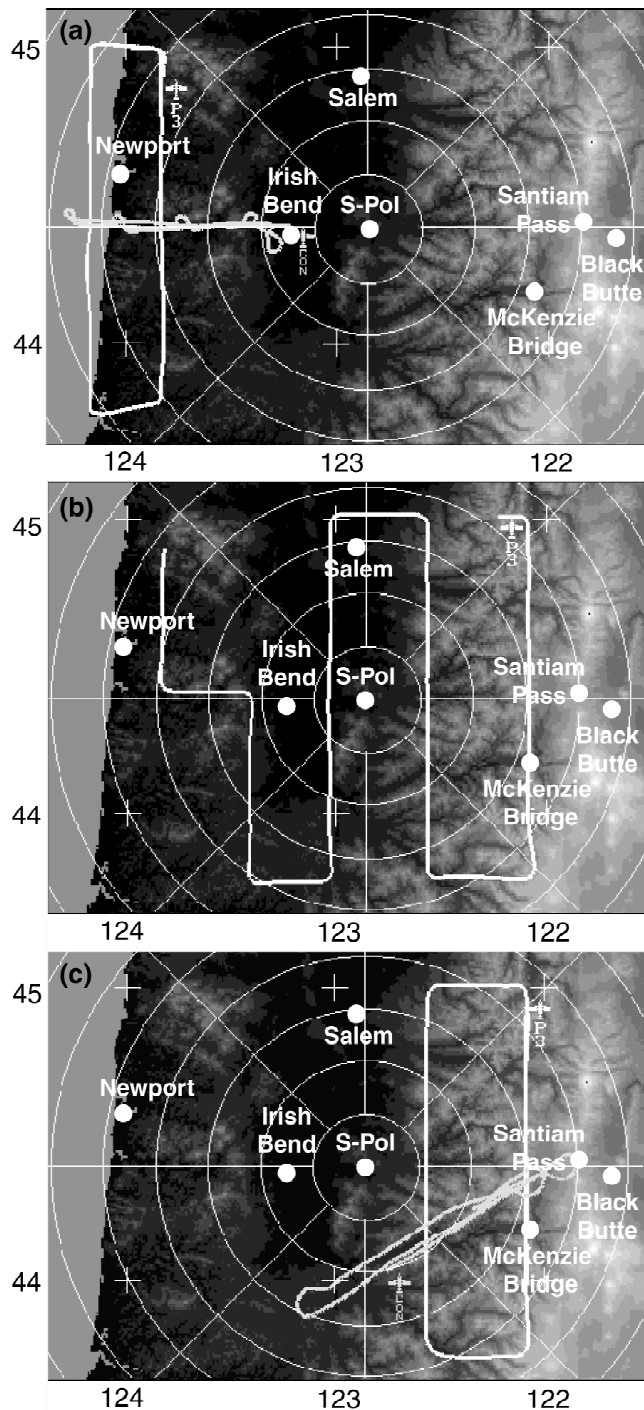


Fig. 1 Flight tracks for NOAA P-3 (white lines) and University of Washington Convair-580 (gray lines) research aircraft during the IMPROVE-2 mission of 8-9 December 2001. Shading indicates terrain height, with the darkest N-S oriented band through Irish Bend locating the Willamette Valley, and lighter shading to east indicating the Cascade Mountains. Panels (a), (b) and (c) refer to roughly the first quarter, middle half, and last quarter, respectively of the P-3's mission.

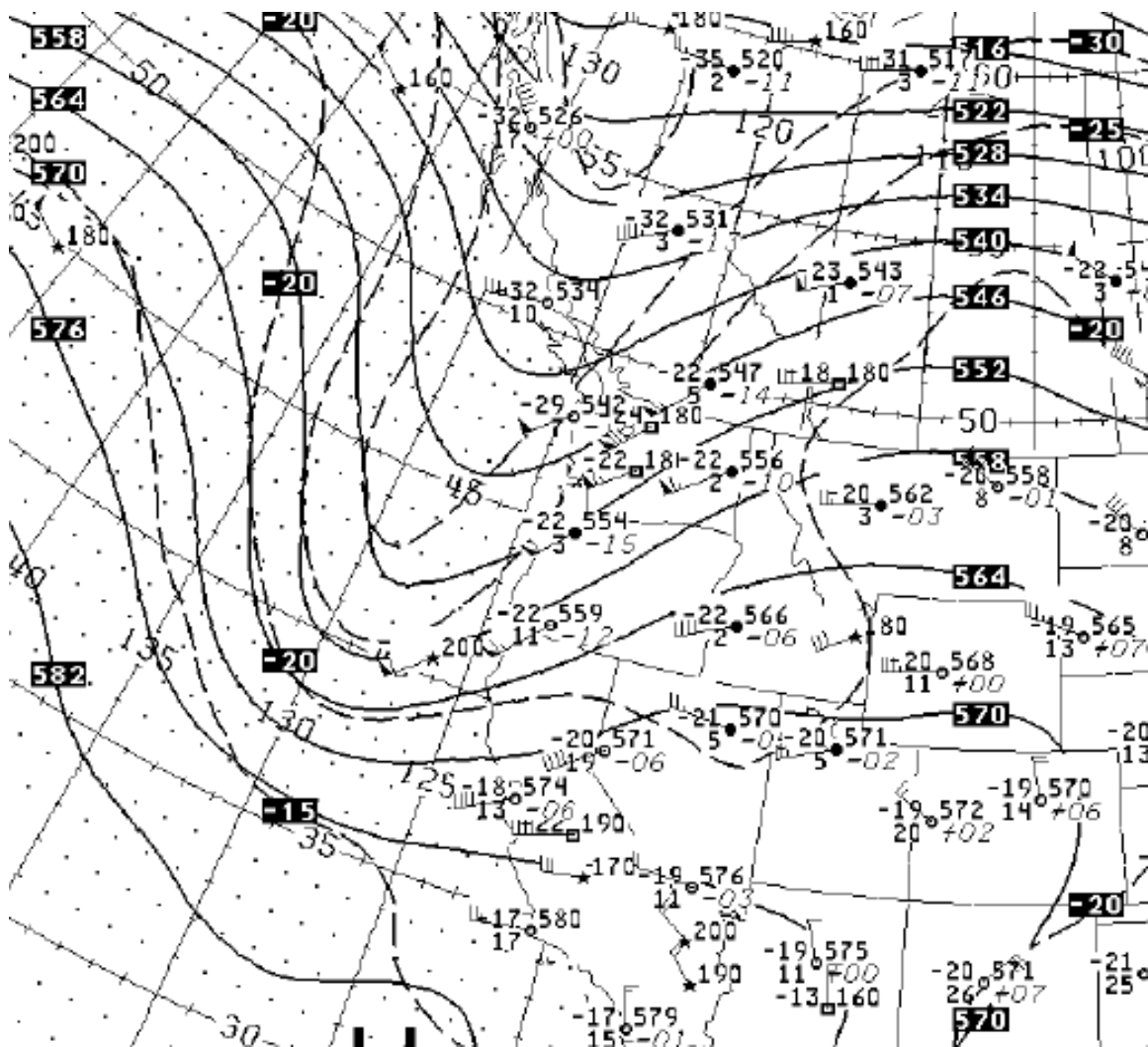


Fig. 2a 500 hPa chart for 0000 UTC 9 December 2001 from the National Centers for Environmental Prediction (NCEP).

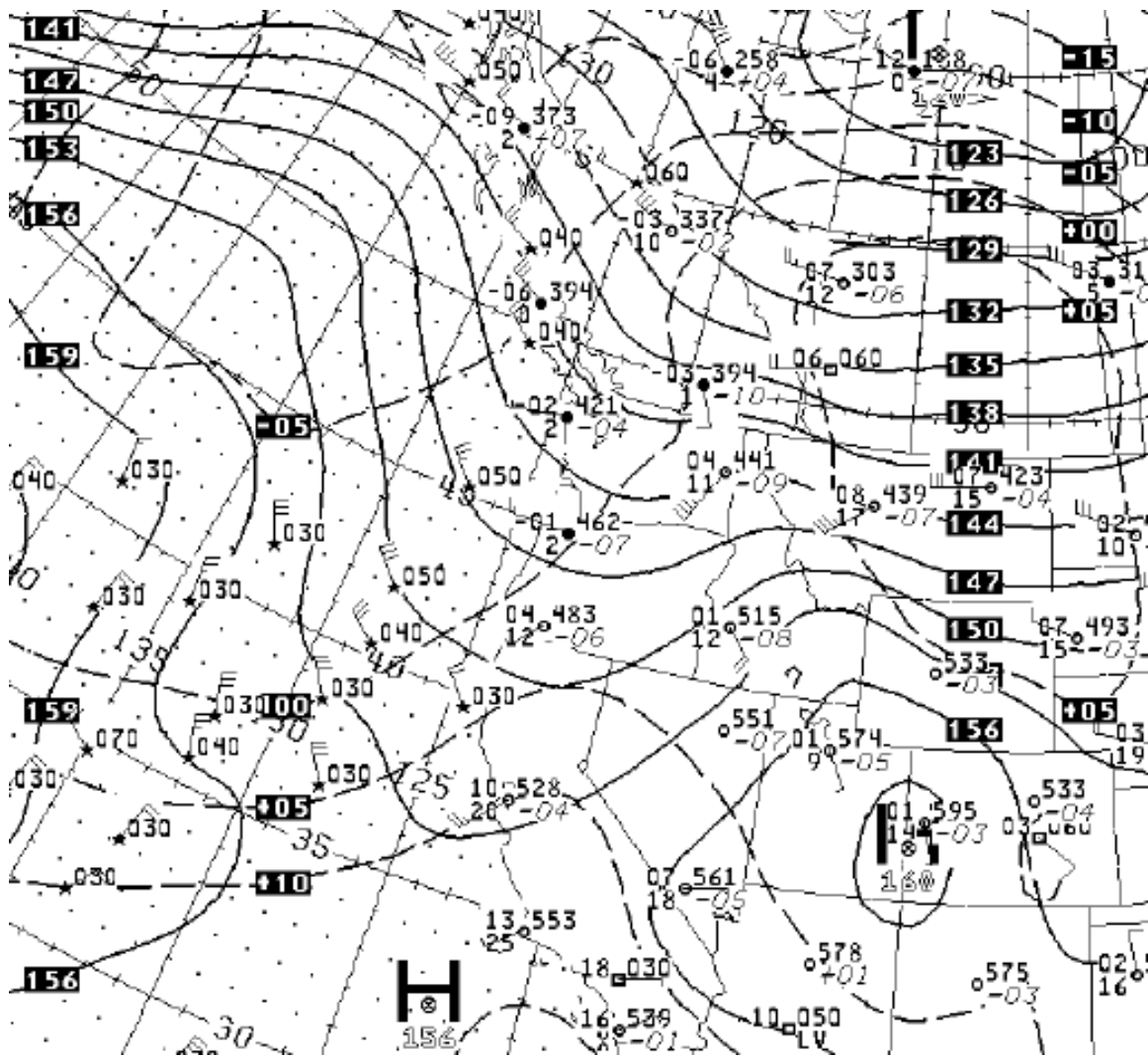


Fig. 2b As in Fig. 2a, but for 850 hPa.

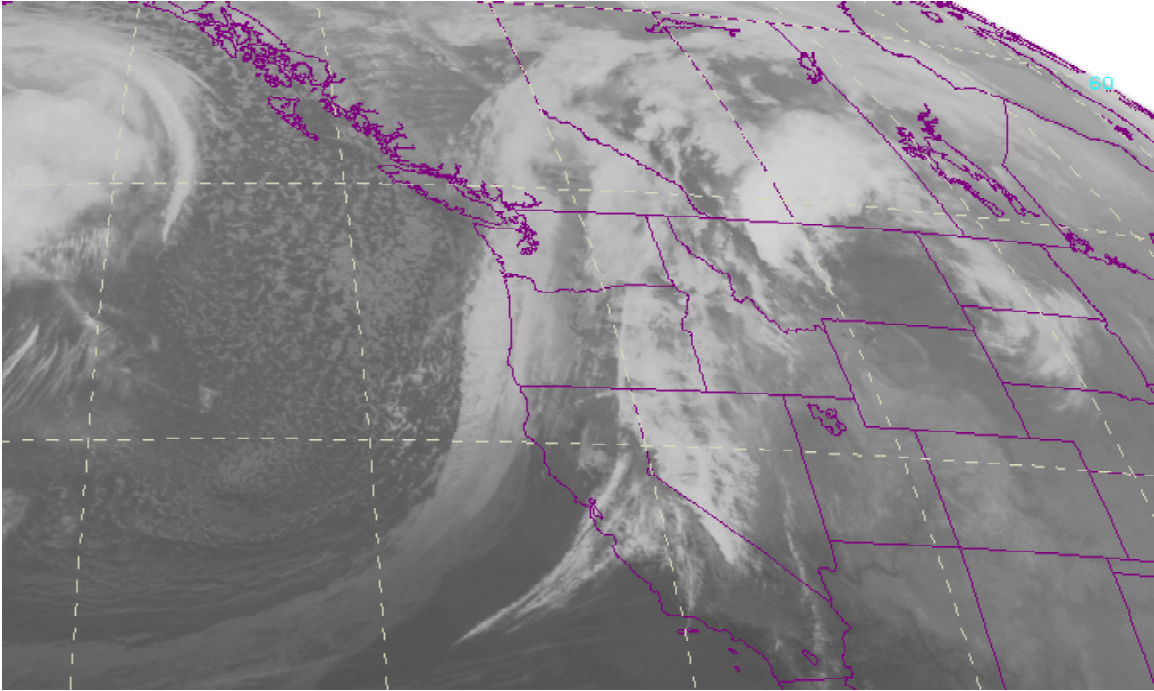


Fig. 3 GOES-W infrared satellite image at 0000 UTC 9 December 2001.

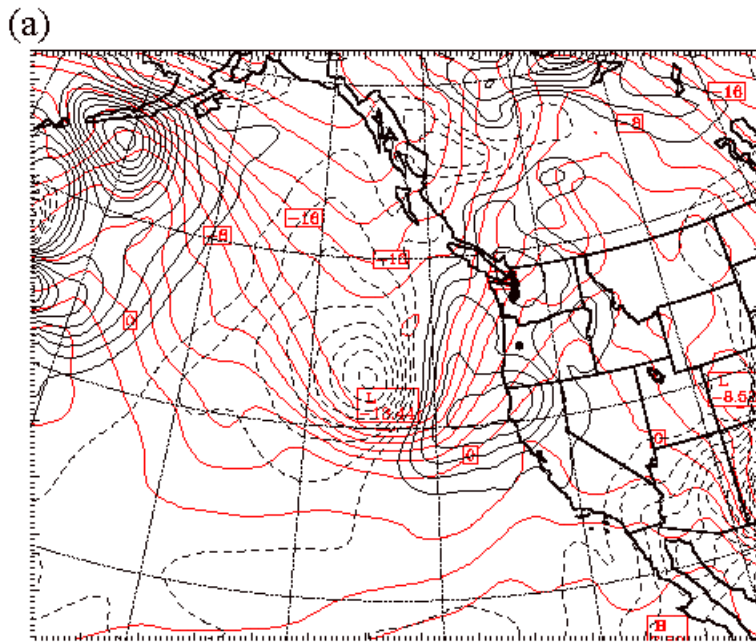


Fig. 4a 700 hPa air temperature ($^{\circ}\text{C}$; red lines) and quasi-geostrophic omega (microbar s^{-1} ; black lines) for 1800 UTC 8 December 2001. Dashed (solid) omega contours indicate positive (negative) values at an interval of $0.5 \text{ microbar s}^{-1}$; zero contour is omitted.

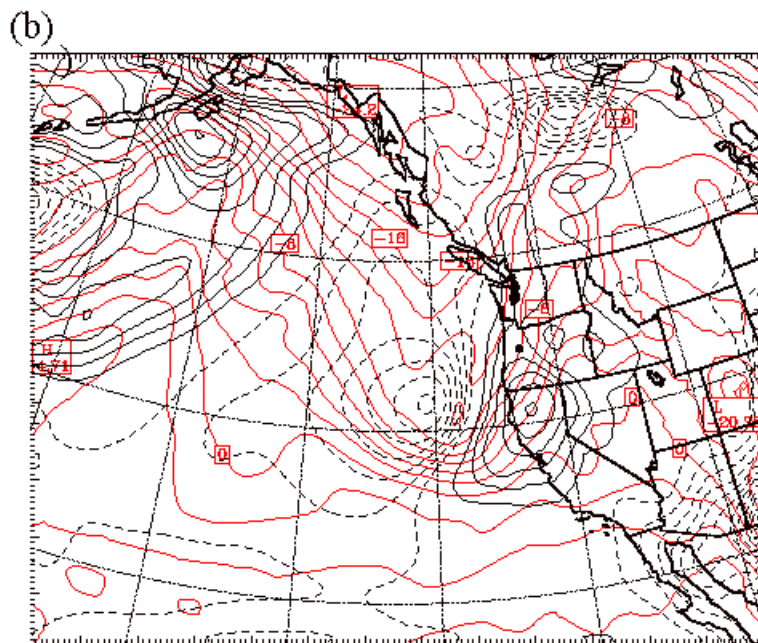


Fig. 4b As in Fig. 4a, but for 0000 UTC 9 December 2001.

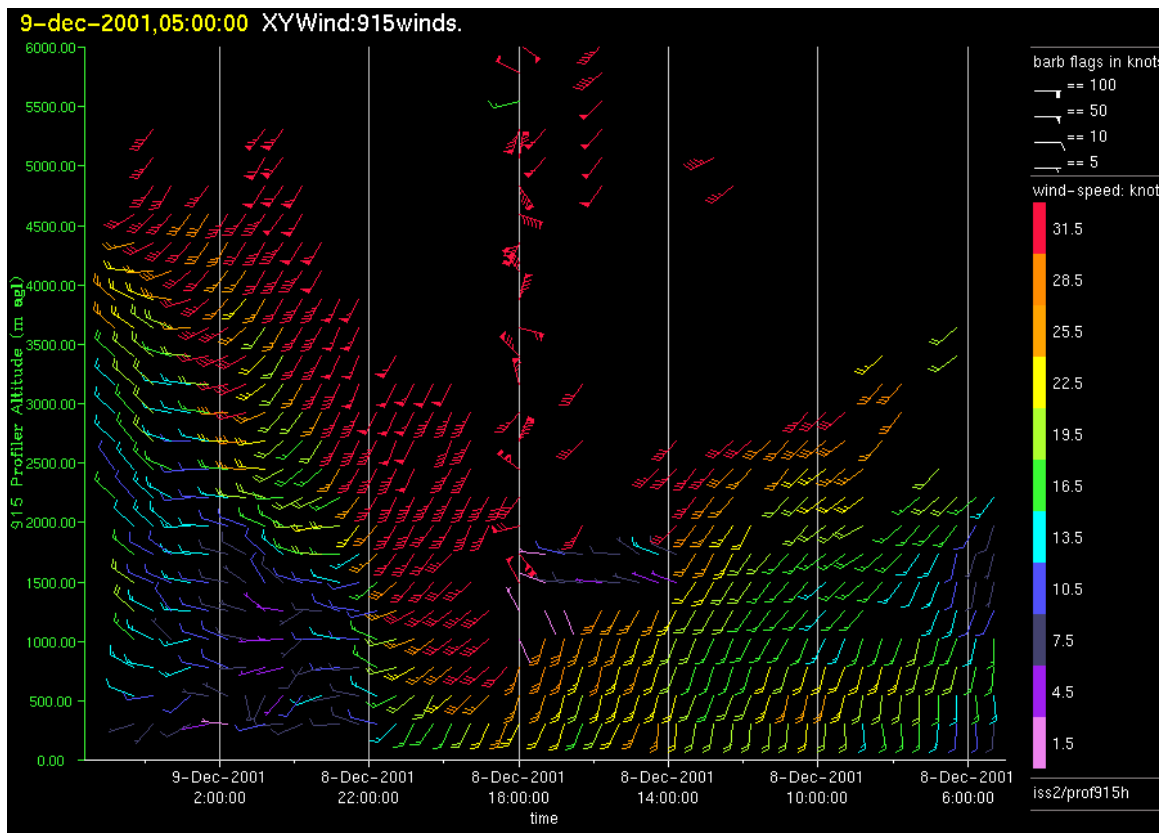


Fig. 5 Time-height section of winds from the 915-MHz wind profiler located at Irish Bend, OR (Lat: 44.36 N, Lon: 123.21 W, Elevation: 85 m). Time runs from right to left.

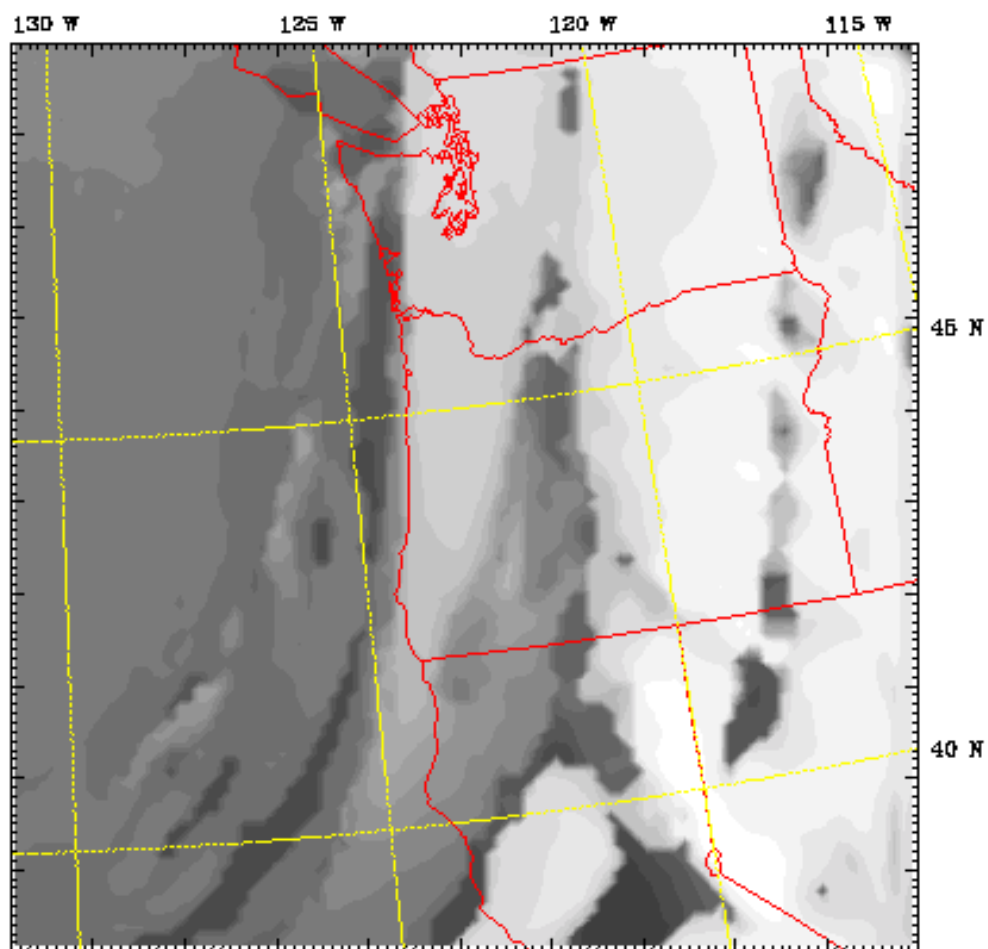


Fig. 6 Simulated IR satellite image valid at 0000 UTC 9 December based on cloud-top temperature from a 24-h forecast of the NCAR/Penn State MM5 numerical weather prediction model.

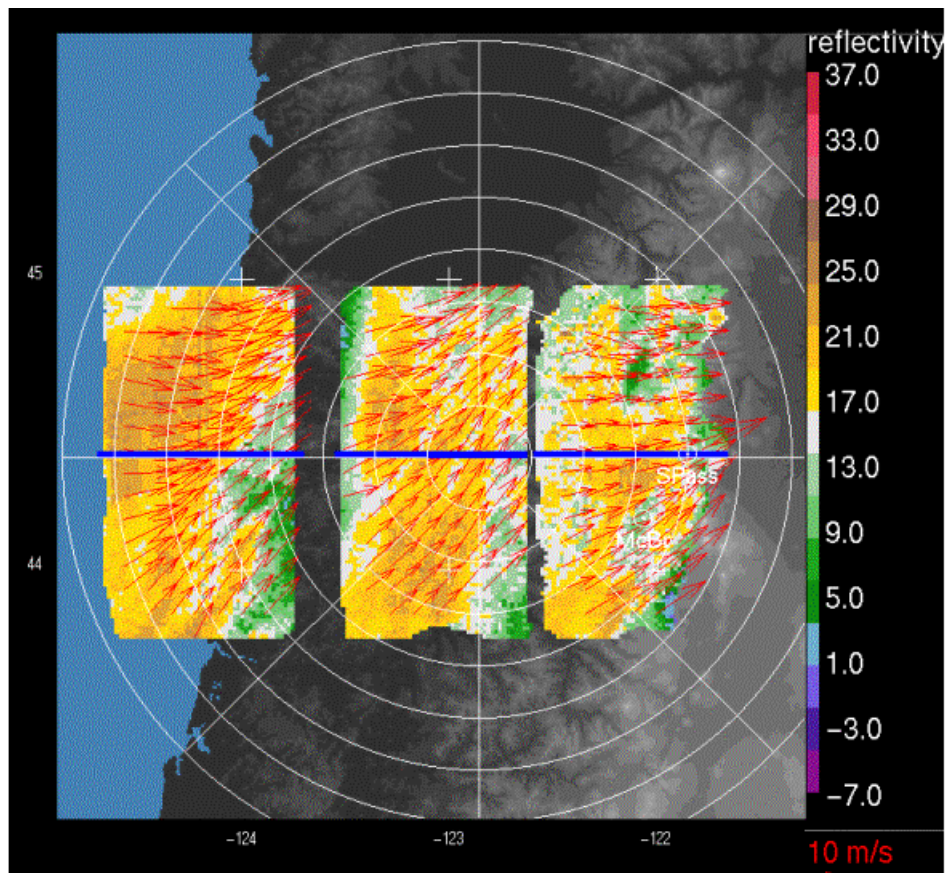


Fig. 7 Plan views of radar reflectivity (dBZ; see color table) and wind vectors at 3 km from the 2225 UTC, 2359 UTC and 0129 UTC 8-9 December radar volumes from the P-3 aircraft. Surrounding topography is shown as in Fig. 1, and range circles (20 km interval) centered on S-Pol radar are plotted for reference

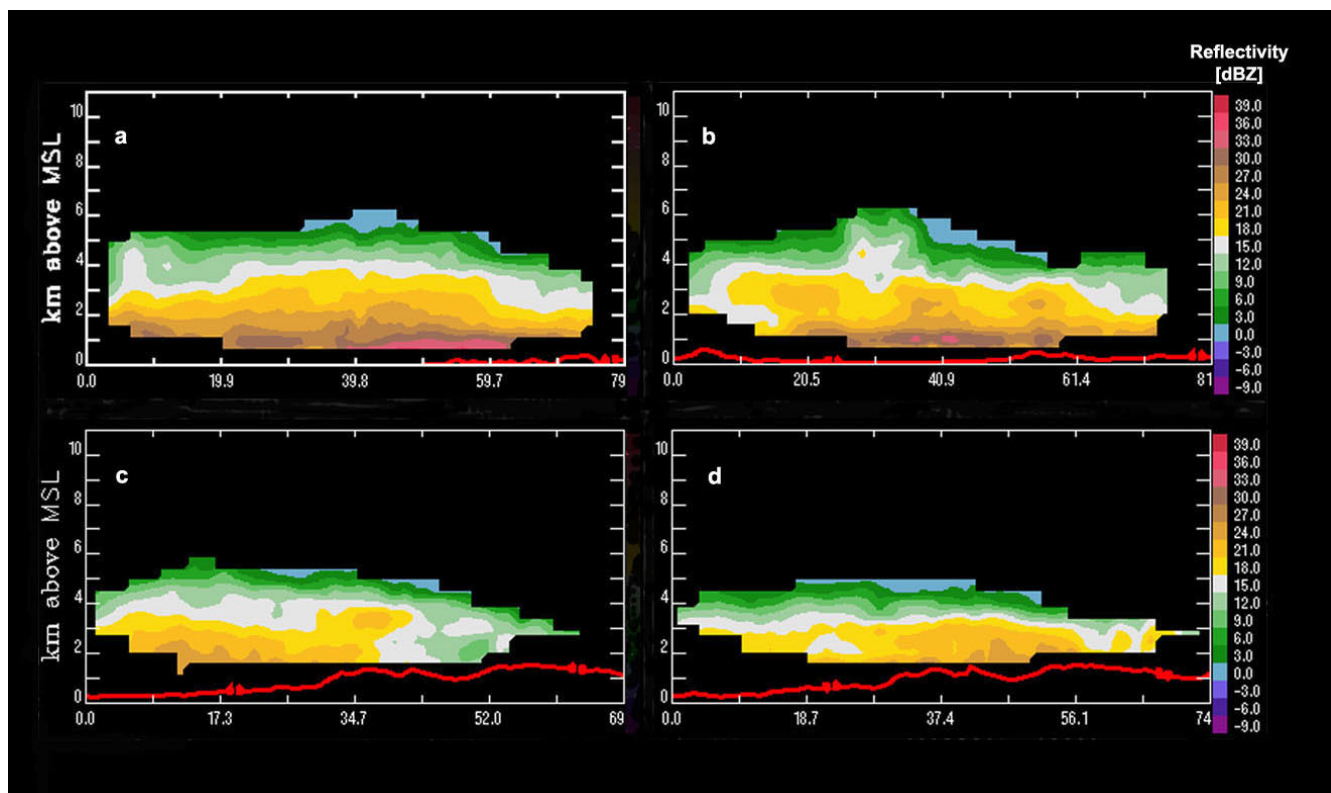


Fig. 8 Vertical cross-sections of radar reflectivity (dBZ) along 44.50 N from the (a) 2315, (b) 2359, (c) 0045 and (d) 0129 UTC P-3 radar volumes on 8-9 December 2001.

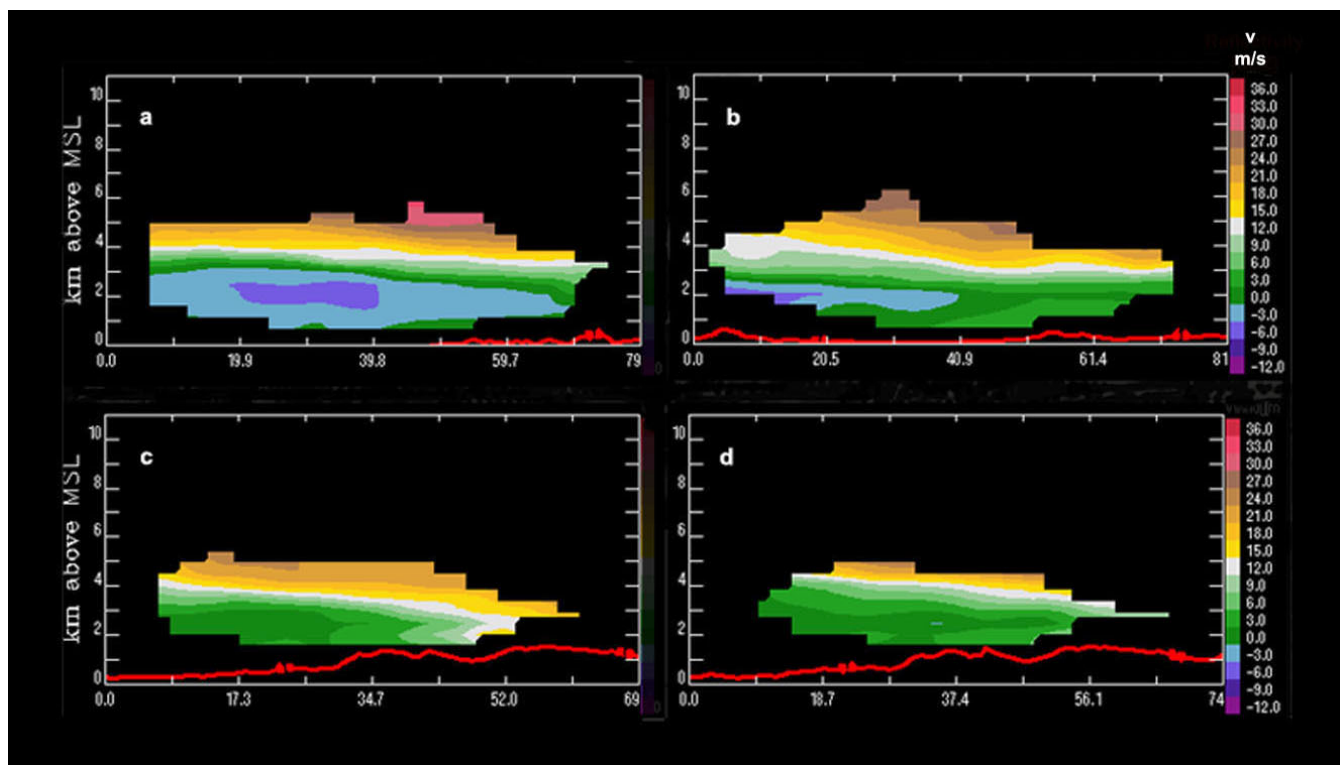


Fig. 9 As in Fig. 8, but for the meridional (v-component) wind (m s⁻¹).

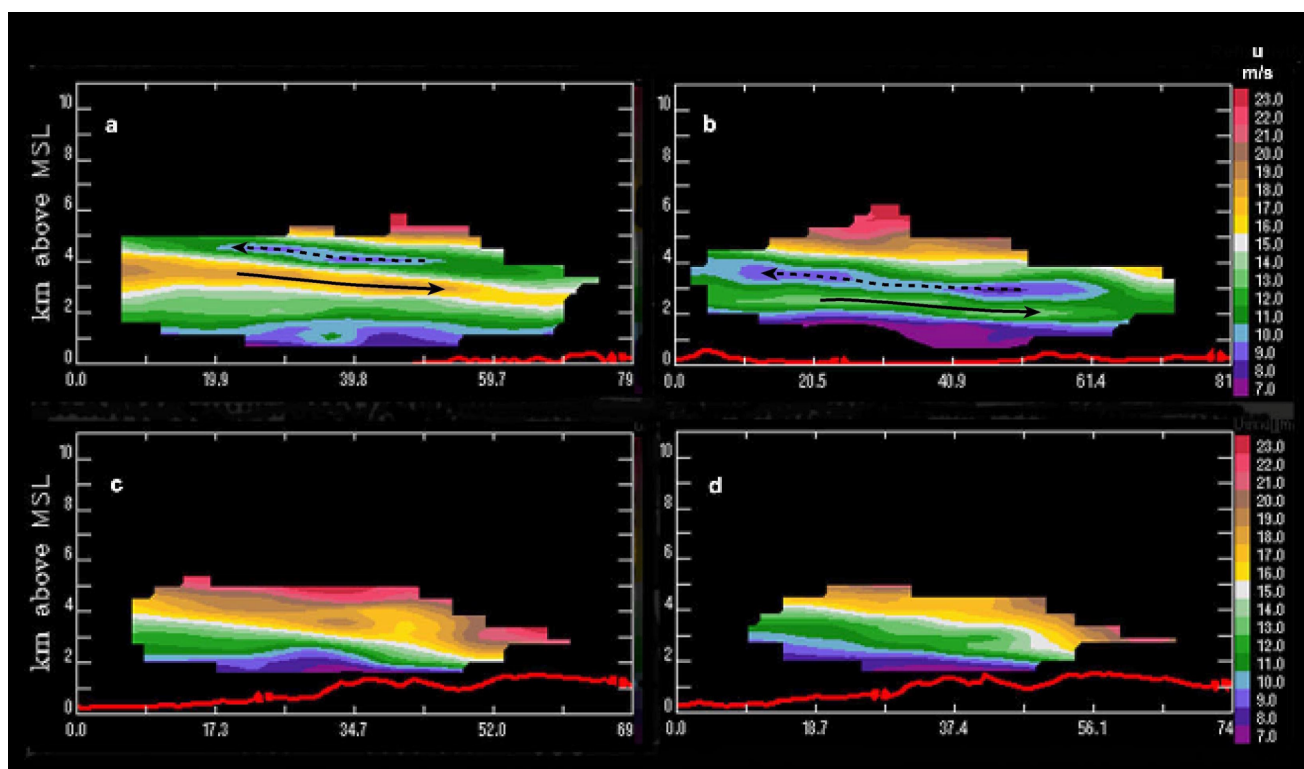


Fig. 10 As in Fig. 8, but for the zonal (u-component) wind (m s^{-1}). Dashed and solid arrows refer to the front-to-rear and rear-to-front components, respectively, of the secondary circulation associated with the WCFR.

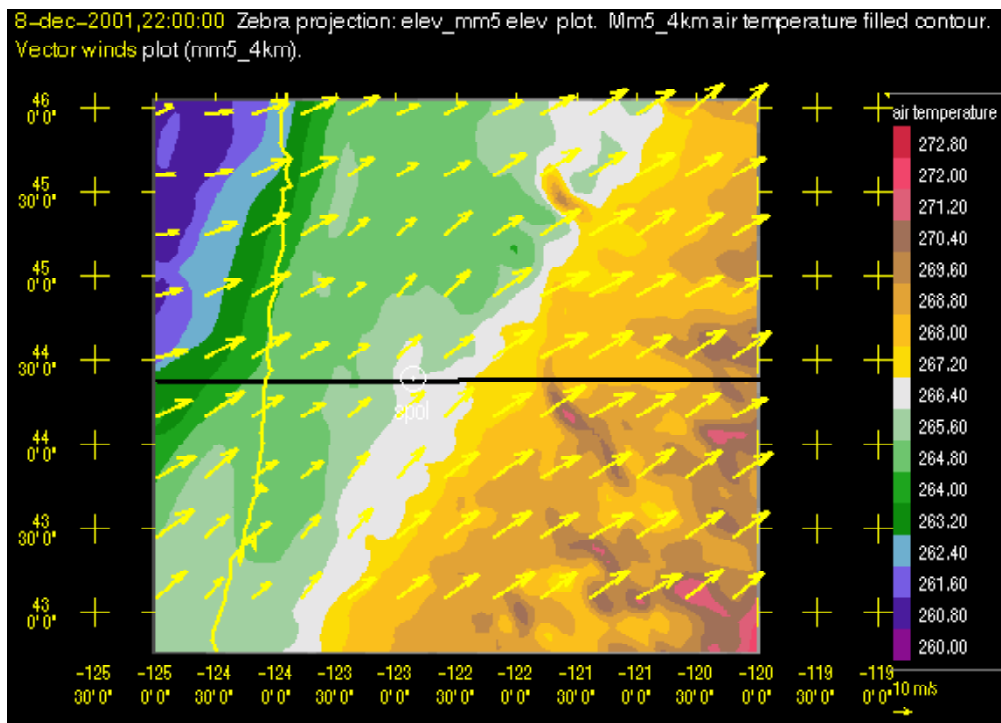


Fig. 11a Air temperature ($^{\circ}\text{C}$) at 3 km at 2200 UTC 8 December from the MM5. Black line indicates projection of vertical cross section shown in Figs. 12-14.

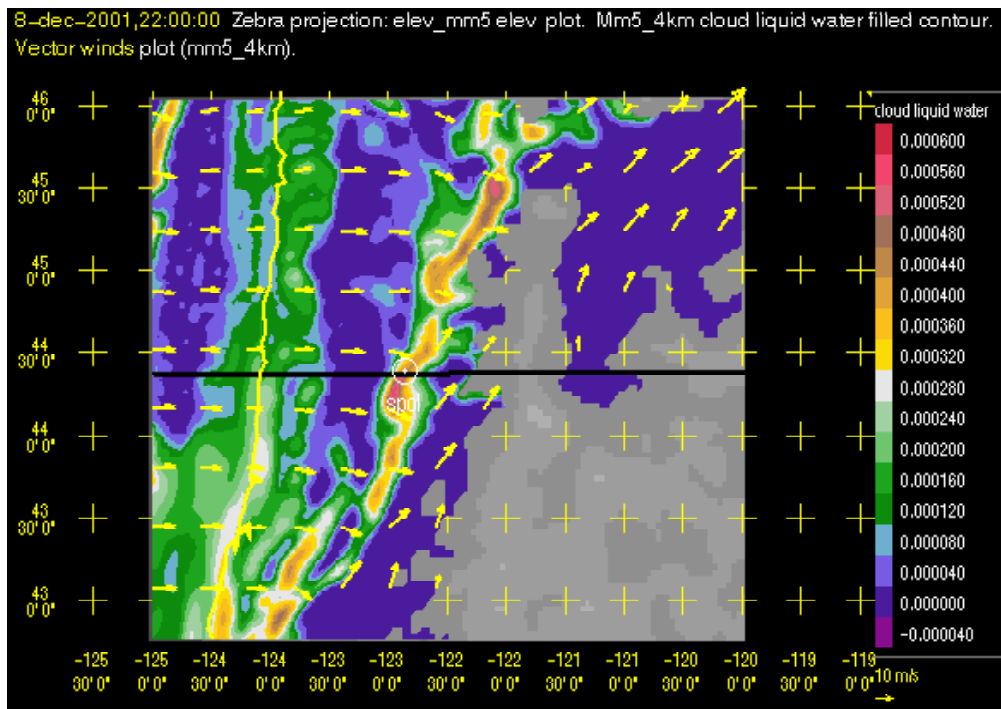


Fig. 11b As in Fig. 11a, but for cloud liquid water concentration (g kg^{-1}) at 1 km.

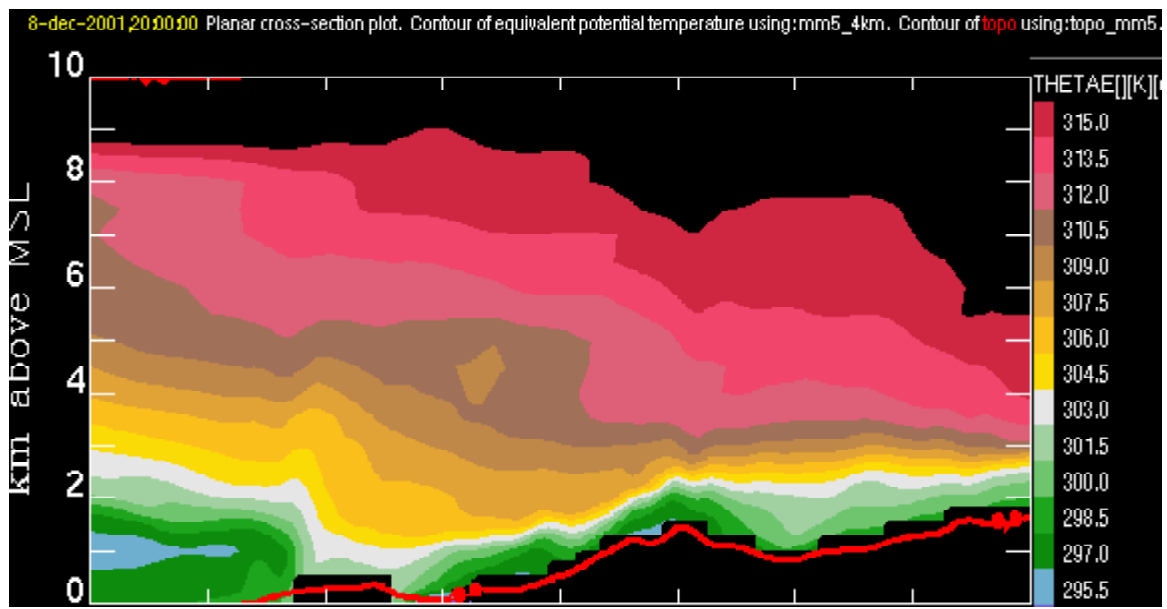


Fig.12a Vertical cross-section of equivalent potential temperature (K) along 44.5 N at 2000 UTC 8 December from the MM5.

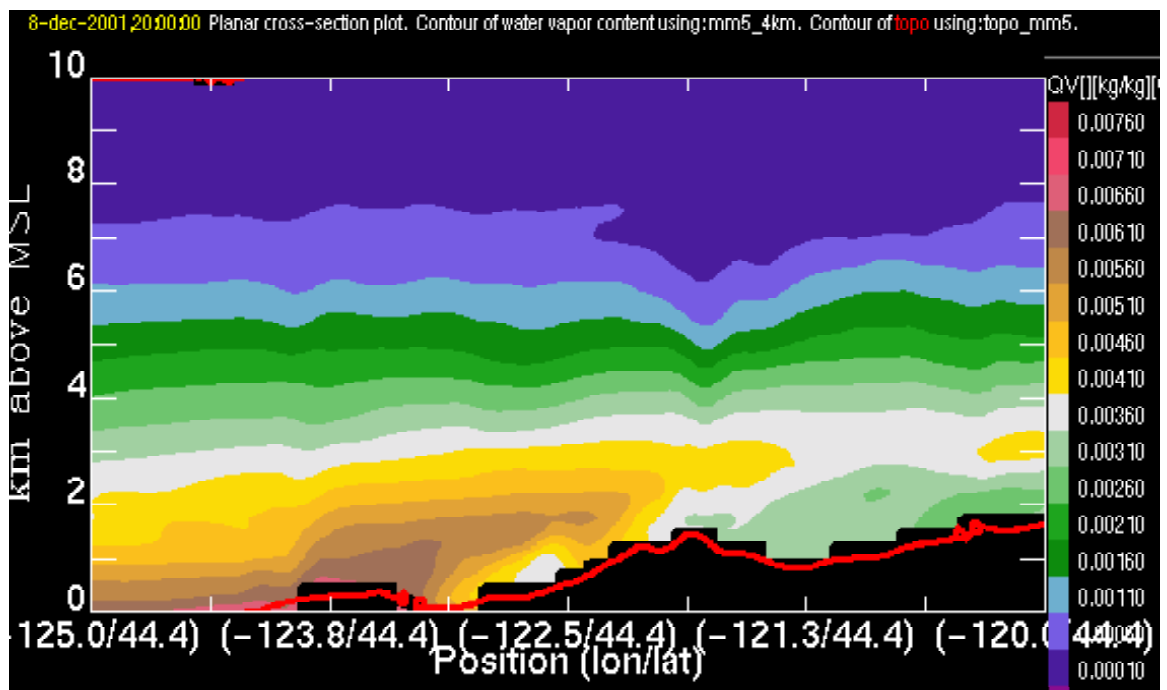


Fig. 12b As in Fig. 12a, but for water vapor mixing ratio (g kg^{-1}).

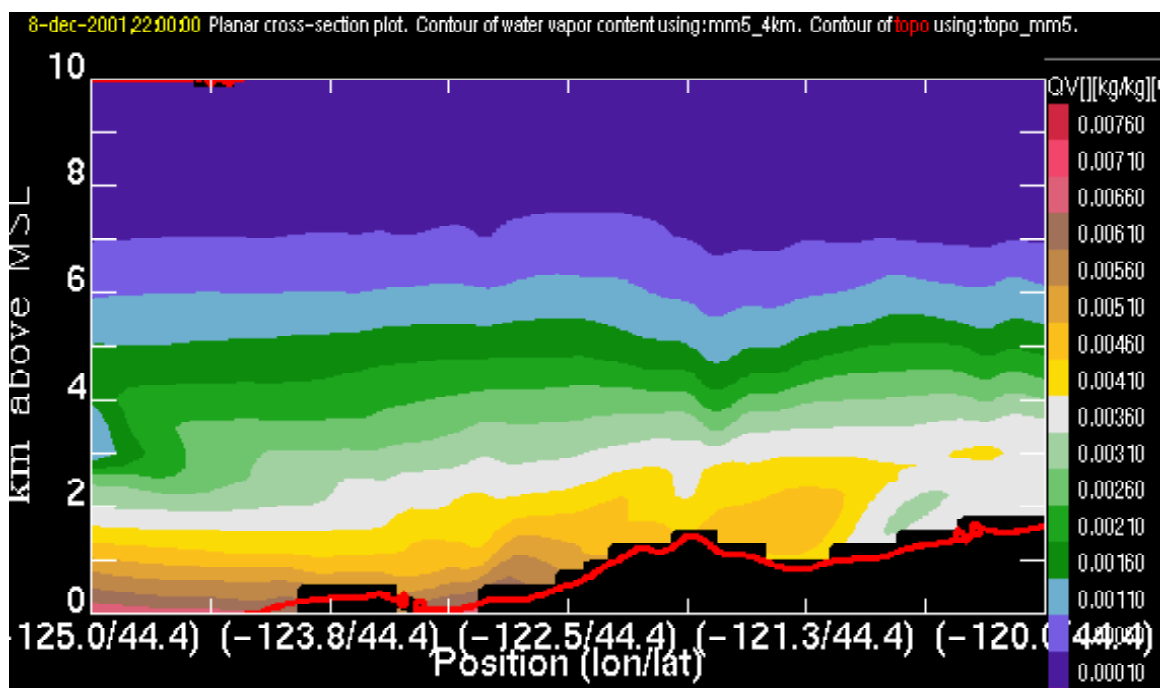
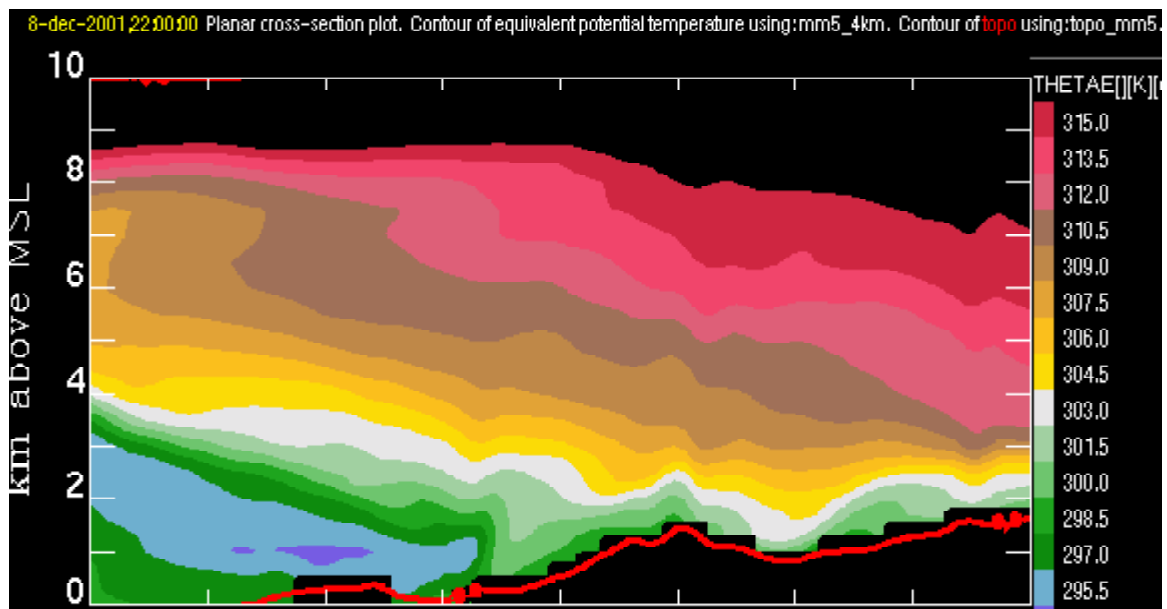


Fig. 13 As in Fig. 12, but for 2200 UTC 8 December.

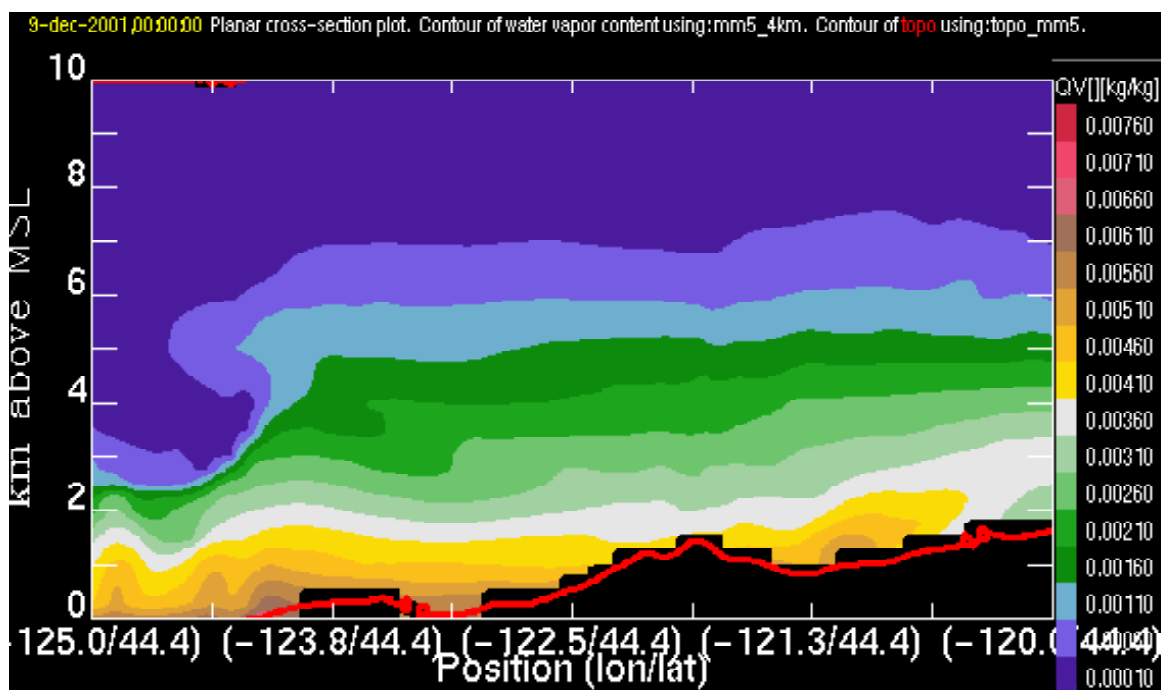
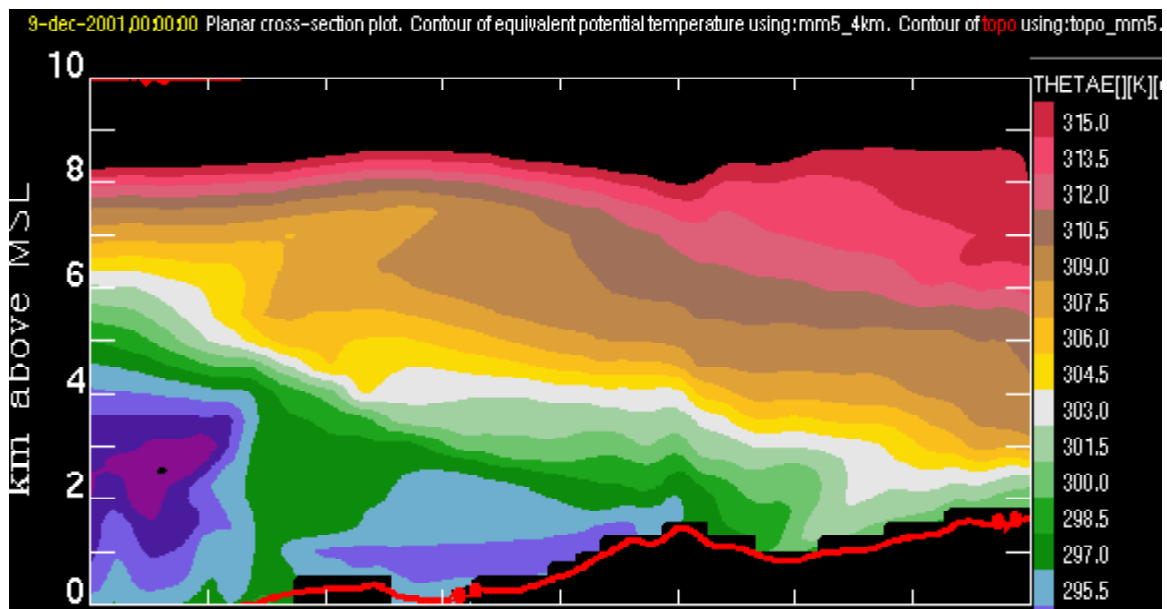


Fig. 14 As in Fig. 12, but for 0000 UTC 9 December.

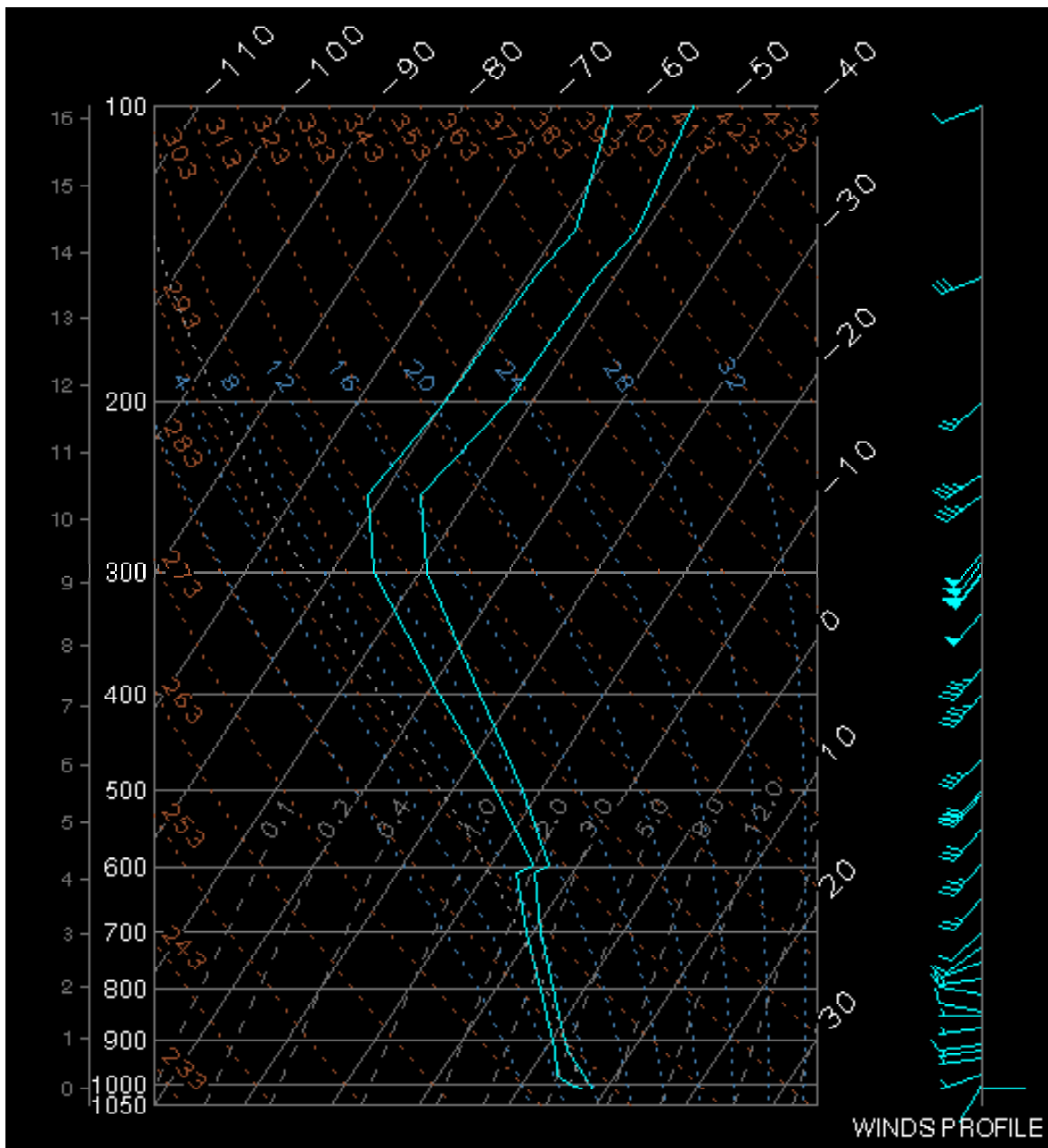


Fig. 15 Skew-T sounding from Salem, OR at 0000 UTC 9 December.

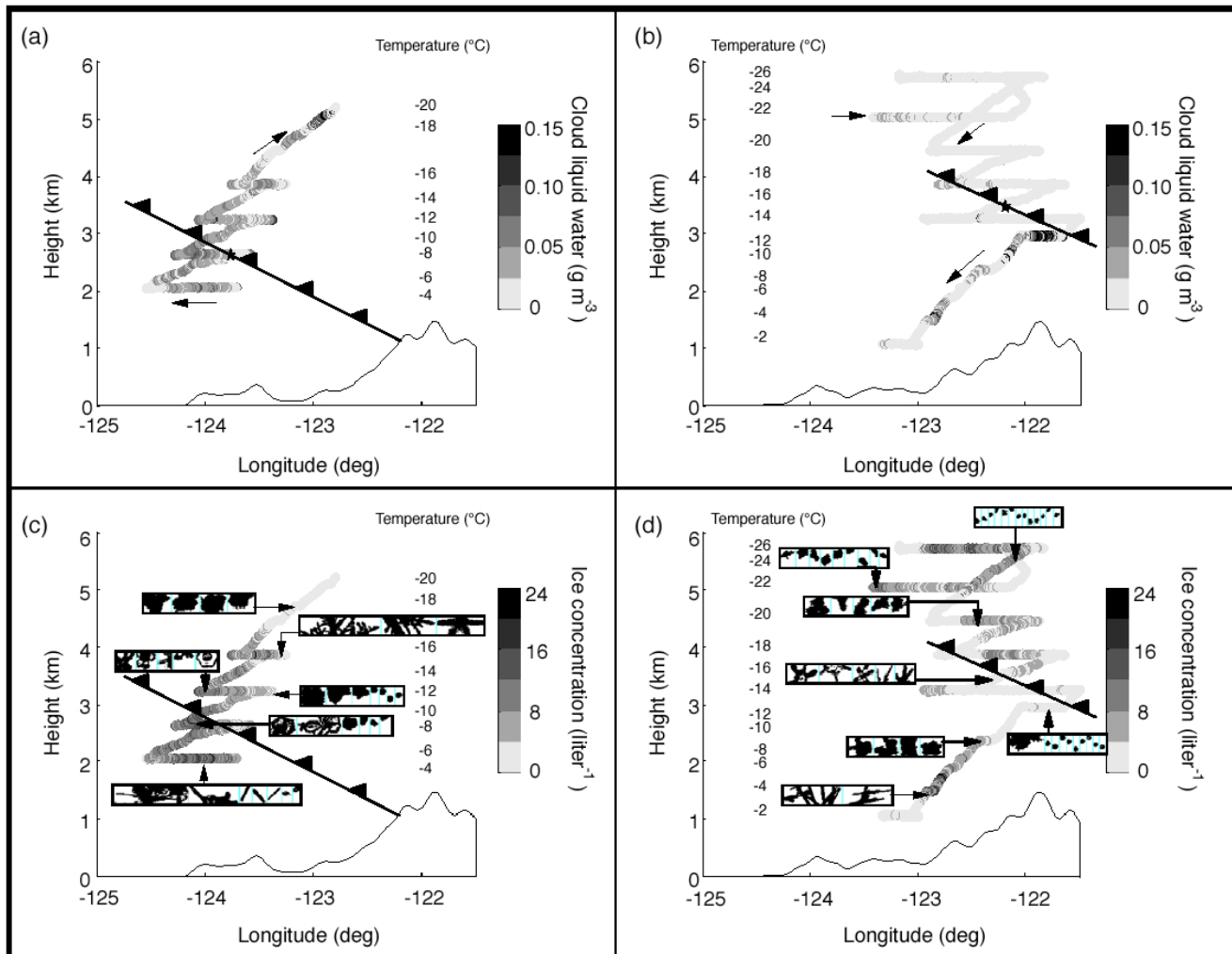


Fig. 16 Flight-level data for the 8-9 December 2001 from the University of Washington's Convair-580 aircraft. (a) Cloud liquid water (g m^{-3}) during the coastal flight (2151-2330 UTC). Flight-level temperatures ($^{\circ}\text{C}$) are also shown. Arrows indicate direction of track. (b) As in (a), but for the Cascade flight (0112-0442 UTC). (c) Ice crystal concentration (liter^{-1}) with sample PMS 2D-C imagery along the coastal flight legs. The vertical dimension of each sample ice crystal image strip is 800 microns. (d) As in (c) but for the Cascade flight.

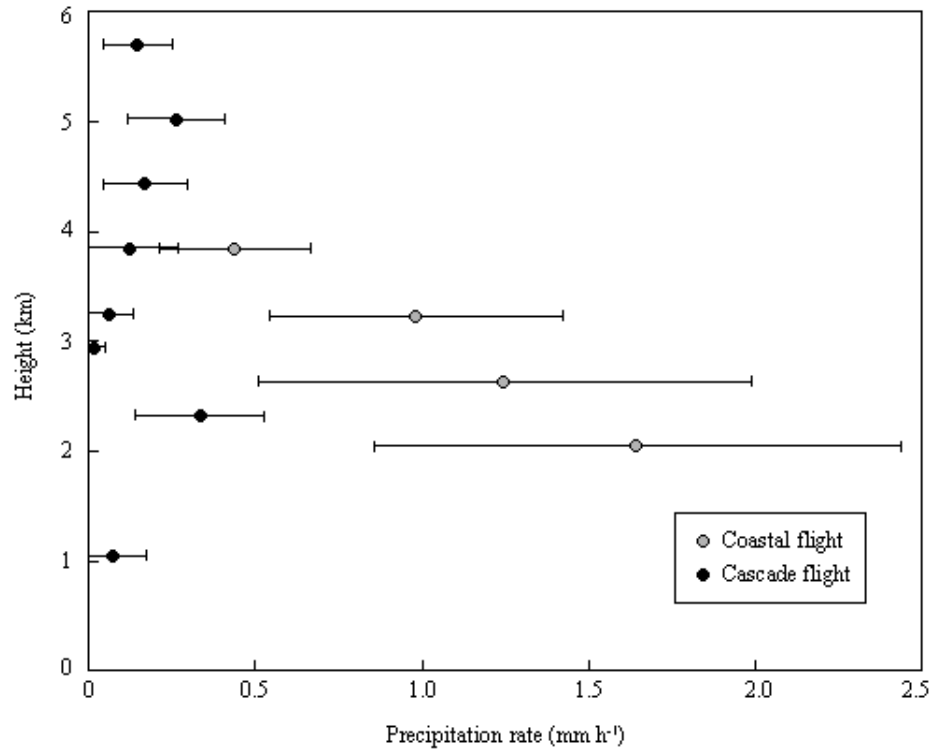


Fig.17. Vertical profiles of precipitation rate (mm h^{-1}) for the Convair-580 Coastal and Cascade flights. Values are obtained for the horizontal flight legs seen in Fig. 16. For each flight leg, dots represent mean values and bars represent one standard deviation.

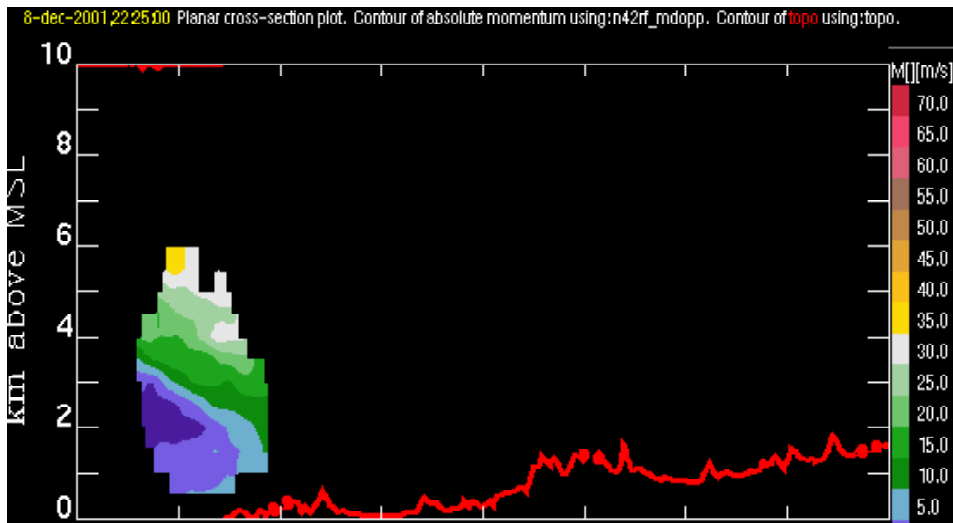


Fig. 18 Vertical cross-section of absolute momentum (m s^{-1}) along 44.50°N from the P-3 airborne Doppler radar analysis at 2225 UTC 8 December.

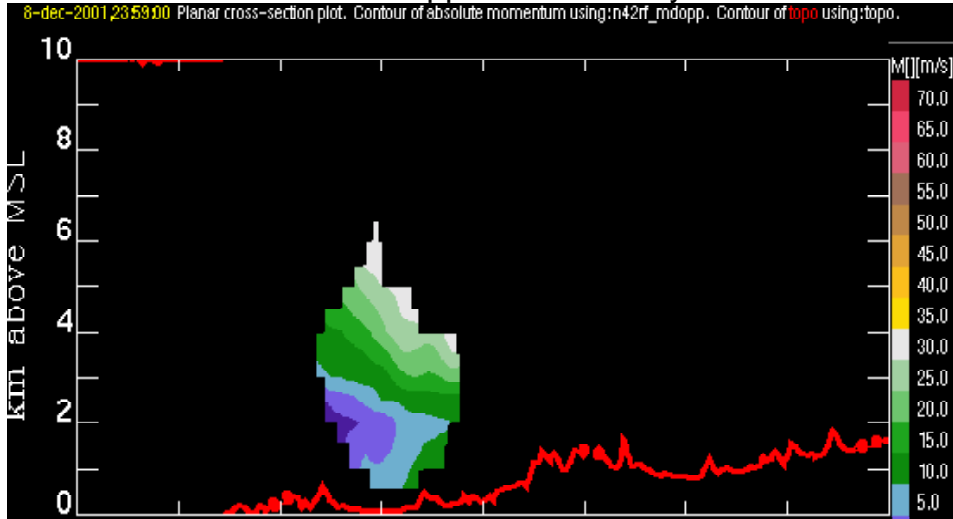


Fig. 19 As in Fig. 18, but for the 2359 UTC analysis.

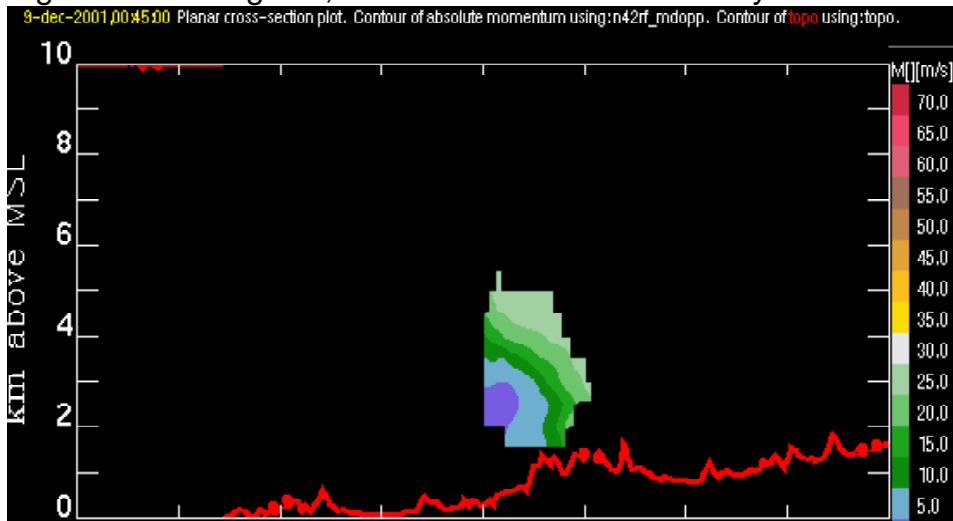


Fig. 20 As in Fig. 18, but for the 0045 UTC analysis.

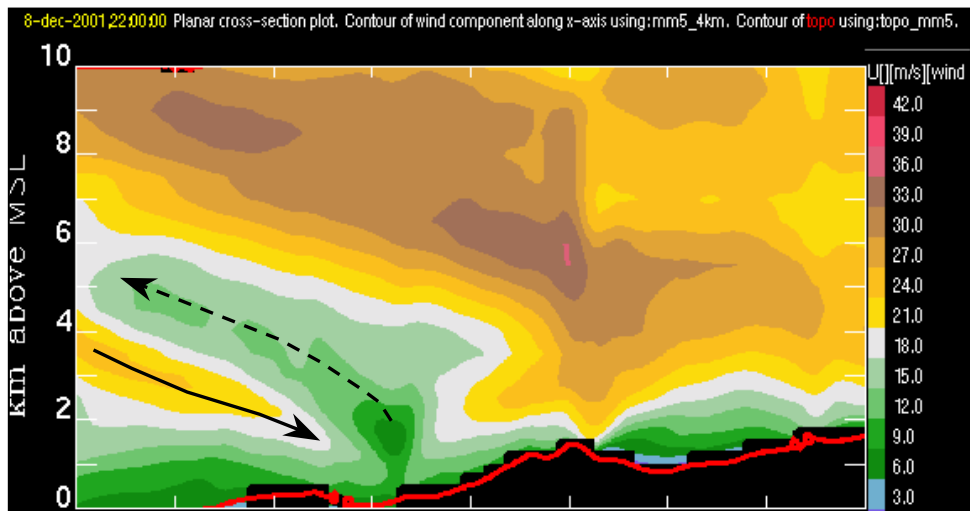


Fig. 21 Vertical cross-section of zonal wind (m s^{-1}) along 44.5 N at 2200 UTC 8 December from the MM5.

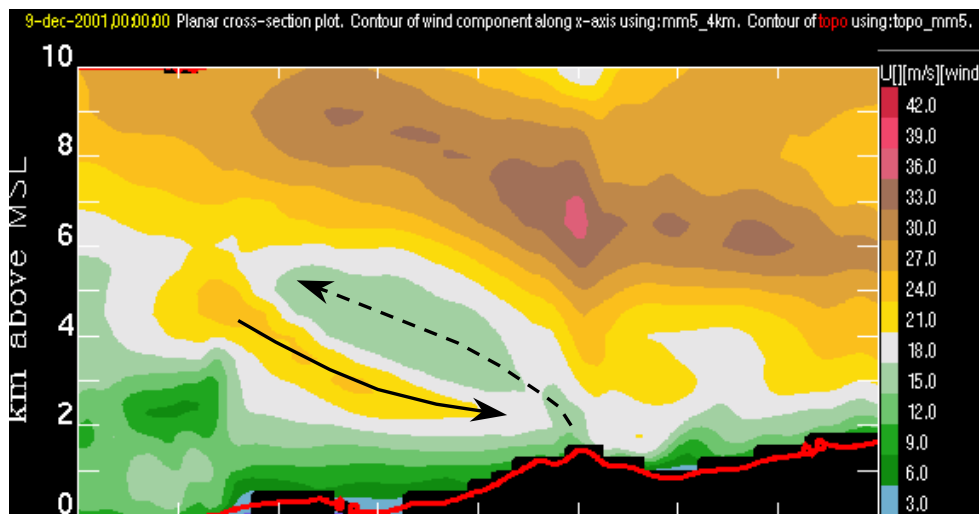


Fig. 22 As in Fig. 21, but for 0000 UTC 9 December.

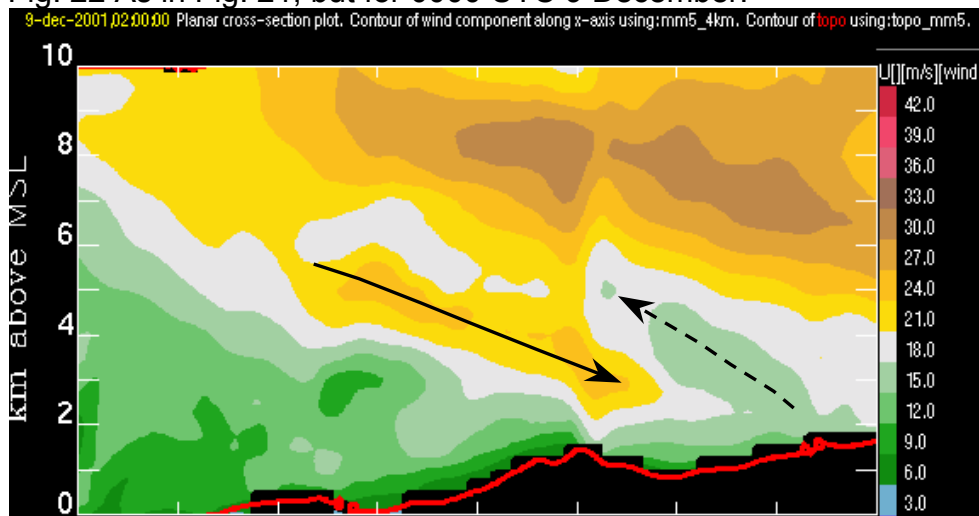


Fig. 23 As in Fig. 21, but for 0200 UTC 9 December.